

RESEARCH ARTICLE | APRIL 27 2023

Numerical simulation of wave propagation in ice-covered ocean environments based on the equivalent-source method

He Tengjiao (何腾蛟); Wang Bin (王斌); Tang Shengyu (唐胜雨); ... et. al



Physics of Fluids 35, 047126 (2023)

<https://doi.org/10.1063/5.0144919>

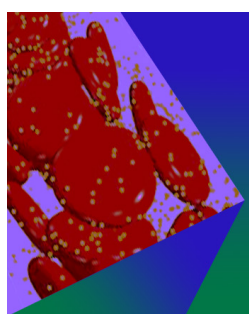


View
Online



Export
Citation

CrossMark



Physics of Fluids

Special Topic: Flow and Forensics

Submit Today!

AIP
Publishing

Numerical simulation of wave propagation in ice-covered ocean environments based on the equivalent-source method

Cite as: Phys. Fluids 35, 047126 (2023); doi: 10.1063/5.0144919

Submitted: 1 February 2023 · Accepted: 6 April 2023 ·

Published Online: 27 April 2023



View Online



Export Citation



CrossMark

Tengjiao He (何腾蛟),^{1,a)} Bin Wang (王斌),^{1,a,c)} Shengyu Tang (唐胜雨),² Fulin Zhou (周富霖),^{1,a)} Shiqi Mo (莫世奇),^{3,b)} and Erzheng Fang (方尔正)^{3,b)}

AFFILIATIONS

¹Key Laboratory of Marine Intelligent Equipment and System, Ministry of Education, Shanghai Jiao Tong University, Shanghai 200240, China

²College of Information Science and Engineering, Ocean University of China, Qingdao 266100, China

³College of Underwater Acoustic Engineering, Harbin Engineering University, Harbin 150001, China

^{a)}Also at: School of Naval Architecture, Ocean & Civil Engineering, Shanghai Jiao Tong University, Shanghai 200240, China.

^{b)}Also at: National Key Laboratory of Underwater Acoustic Technology, Harbin Engineering University, Harbin 150001, China.

^{c)}Author to whom correspondence should be addressed: bin_wang@sjtu.edu.cn

ABSTRACT

Accurate modeling of sound propagation in ice-covered ocean environments can help with interpreting discrepancies between predictions and experimental observations in the changing Arctic Ocean; this is advantageous for environmental conservation, resource exploration, and naval applications. Building on the recent development of the equivalent-source (ES) method (ESM), herein, an ESM-based sub-ice model (ESM-SUBICE) is presented for wave propagation in an ice-covered ocean acoustic environment. The presented model solves exact governing equations for acoustic–elastic propagation in an ice-covered waveguide by expressing the wave solution in terms of a field superposition produced by several sets of ESs. Their unknown amplitudes are solved by strictly enforcing additional ice-layer boundary conditions. ESM-SUBICE achieves high efficiency using a water–seabed Green’s function to automatically satisfy the boundary conditions at this interface. By further dividing the ocean environment into layers, ESM-SUBICE is extended for more general situations including stratified sound-speed structures and seabed range dependencies. ESM-SUBICE is benchmarked against a finite-element model, and it is found to produce high-quality solutions with high efficiency. Transmission-loss predictions for elastic, fluid, and free-surface ice representations in different ocean environments are compared to examine the effect of ice elasticity on propagation and scattering. The results suggest that the fluid representation is adequate for deep-water environments where the seabed is soft and the surface duct effect is insignificant; otherwise, for accurate predictions, the ice elasticity should be considered.

Published under an exclusive license by AIP Publishing. <https://doi.org/10.1063/5.0144919>

I. INTRODUCTION

Recent years have seen increased concern about the acoustic environment in the ice-covered Arctic Ocean.^{1–4} Various types of natural source contribute to this noise, including marine fauna,^{5,6} earthquakes,⁷ ice movements,^{8,9} and iceberg collapse.^{10,11} There are also many anthropogenic noise sources in this region, including those induced by resource exploration,¹² scientific investigations,^{13–16} and naval activities. Furthermore, the acoustic field is complicated by the interaction of sound waves with the ice cover, which not only reflects sound but also transfers acoustic energy to elastic waves traveling along the ice.¹⁷ Being able to accurately model sound propagation in an ice-covered ocean environment is beneficial

for acoustically monitoring underwater activities and mitigating anthropogenic noise to protect marine fauna from adverse impacts.

Nevertheless, accurately modeling sub-ice sound propagation requires consideration of the ice cover’s elastic characteristics, including reflectivity, loss mechanisms, and range-dependent thickness. Compared to a common ocean scenario with a pressure-release surface, this makes the modeling work challenging. The acoustic–elastic interactions at the ice–water interface involve reflection, transmission, energy conversion between compressional and shear waves, and re-radiation back to the water column.^{17,18} When the ice-layer thickness varies with propagation range due to seasonal changes, the acoustic–elastic interactions can be complicated further, as acoustic modal cut

off and leaky-elastic-wave behaviors may occur. Therefore, the elasticity of the ice should be carefully considered in any sub-ice propagation model to accurately predict received sound levels in a sub-ice ocean channel.

The current models for sub-ice sound propagation can be divided into two branches. The first treats the ice layer as a reflective interface such that the acoustic interaction with the sea ice can be modeled using an effective reflection coefficient. Examples include: ray models,^{19,20} which involve a high-frequency, asymptotic approximation of the wave solution to the Helmholtz equation; and the perturbation method,²¹ which is based on the normal mode theory. Ray models are highly efficient and capable of dealing with range-dependent problems. However, their accuracy for sub-ice sound propagation depends on the model that is used for the ice–water reflection coefficient; this is inadequate for proper modeling of acoustic–elastic behaviors, as ray models do not include the elastic wave field.

The second broad class of model directly considers the solid elastic characterization of the sea ice and couples the solid mechanics and pressure acoustics by enforcing proper fluid–solid boundary conditions. Collis *et al.* used the elastic parabolic equation (PE)—a classic method widely applied in underwater acoustics—to model sub-ice sound propagation;²² they derived rigorous governing equations for seismo-acoustic propagation in a stratified ice-covered ocean and generated evolutionary solutions in the solid and the fluid using the paraxial approximation. The elastic PE is numerically efficient and versatile for handling sound-speed inhomogeneities; however, one-way solutions provided by the elastic PE are inadequate when back-scattering is significant, especially for reverberation modeling.²³ Additional numerical treatments are, thus, required to obtain two-way PE solutions,^{24,25} and this undoubtedly intensifies the computational cost.

There are also fully numerical methods for modeling sub-ice sound propagation. The finite-difference method (FDM), for instance, has been used to interpret frequency-dependent behaviors of the scattered field from a rough ice layer.²⁶ Additionally, the finite-element method (FEM) has been used to investigate the possibility of replacing the elastic ice cover with a pressure-release surface in the modeling of sub-ice reverberation.¹⁸ Both the FDM and FEM are highly versatile, as they are fully customizable in terms of the media properties and boundary geometries considered in the simulations. These methods provide solutions that converge to the exact wave solution, and they can, thus, be used as benchmarks for other approaches. Nevertheless, their main drawback is the massive computational burden that results from their basis in volume discretization. As an alternative, many researchers have attempted to reduce computational complexity by simplified modeling of the elastic layer as an effective fluid²⁷ or a pressure-release surface;²⁸ this has enabled many acoustic-propagation models to handle the sub-ice situation.^{29–31} However, using an effective approximation of the ice cover can result in discrepancies from experimental observations (in general, higher received sound levels). This is because the ice cover's reflectivity tends to be overpredicted, especially when rough ice–water interfaces are considered.²¹

In this work, we sought to develop a numerical model that provides benchmark-quality solutions but solves the exact governing equation for acoustic–elastic propagation more rapidly than volume-discretization-based approaches. Boundary-integral-based methods are promising candidates to achieve this goal because they explicitly

solve the wave equation by only discretizing the treated boundaries. Examples of such approaches include the boundary-element method (BEM) and the equivalent-source method (ESM);³² each of these has demonstrated its ability to solve complex ocean acoustic problems.^{33–39} However, ESM outperforms BEM in terms of its simpler numerical implementation and the avoidance of a singularity in Green's function.³²

Here, we present an ESM-based sub-ice model (SUBICE), namely, ESM-SUBICE, for sound propagation in an ice-covered ocean environment. Exact governing equations for acoustic–elastic propagation are established, strictly enforcing the zero-traction condition at the air–ice interface and the continuity and zero-shear stress conditions across the ice–water interface. ESM-SUBICE solves the exact wave equation by expressing the solution in terms of the field superposition by equivalent sources (ESs) with unknown amplitudes. Five sets of ESs are used to replace the primary (P) and secondary (S) waves excited by sound: those reflected by the air–ice interface and those reflected by the ice–water interface. To handle more general situations, including sound-speed inhomogeneities in the water column, the ocean is divided into layers in which the sound speed is piecewise constant. Each water layer requires two sets of ESs, one above and the other below the layer's upper and lower interfaces, respectively, to replace the reflections by the adjacent layers. The final set of ESs is chosen to satisfy the water–seabed Green's function,^{40,41} automatically enforcing the continuity of pressure and normal displacement across this interface. In doing so, ESM-SUBICE achieves additional numerical efficiency without actually deploying the ESs that are used to deal with the water–seabed interface. A global coupling linear system is, thus, assembled by imposing the ice-layer boundary conditions and the continuity conditions across all adjacent water layers, through which all ES amplitudes can be solved.

ESM-SUBICE is benchmarked against FEM; solutions are generated for the elastic, fluid, and free-surface ice representations in different underwater environments to establish baseline comparisons of the transmission losses (TLs) in these settings and to discuss the applicability of effective ice representations. Wavenumber-spectrum analyses are presented to interpret the effect of ice elasticity on propagation and scattering from the modal perspective. Furthermore, ESM-SUBICE is used to obtain time-domain solutions via the Fourier synthesis to qualitatively investigate scattering from the rough ice–water interface.

The remainder of this paper is organized as follows: Sec. II presents the mathematical formulation of the methods, Sec. III presents the results of the numerical simulations, and conclusions are drawn in Sec. IV.

II. METHODS

The following analysis considers the exact wave equations governing the acoustic–elastic propagation in an ice-covered waveguide. The governing equations are given in terms of scalar and shear potentials, which are equivalent to those based on the displacement field. Subsection 1 of the Appendix gives the derivation of the potential-based wave equations from the exact governing equations of displacement field. The frequency formulations are presented, with time convention $e^{j\omega t}$, where ω is the angular frequency, t is the time, and $j = \sqrt{-1}$. All the quantities represented by upper-case bold letters are matrices, and those by lower-case bold letters are vectors.

A. ESM-SUBICE for the wave propagation in an ice-covered stratified ocean waveguide

As shown in Fig. 1, we consider a multi-layer ocean waveguide covered by a range-dependent, elastic ice layer. The waveguide is divided into $I+1$ layers. A fluid seabed is assumed here for simplicity. We specify the ice cover to be the zeroth layer. The ice compressional and shear wave speeds are $c_p = \sqrt{\frac{\lambda_{sh} + 2\mu}{\rho_{ice}}}$ and $c_{sh} = \sqrt{\frac{\mu}{\rho_{ice}}}$, respectively, where λ_{sh} and μ are the Lame constants, and ρ_{ice} is the ice density. The water column is of $I-1$ layers, and the i th layer ($0 < i < I$) has a sound speed of c_{wi} and a density of ρ_{wi} . The I th layer is the fluid seabed of sound speed c_s and density ρ_s . The upper and lower boundaries of the i th layer are placed at \mathbf{r}_{bi} and \mathbf{r}_{bi+1} , respectively. The Helmholtz equations governing the scalar potentials, $\Phi_p(\mathbf{r})$ in the ice, $\Phi_{wi}(\mathbf{r})$ in water, and $\Phi_s(\mathbf{r})$ in the seabed, and the shear potential, $\Psi_{sh}(\mathbf{r})$ in the ice, are given by

$$\begin{cases} [\nabla^2 + k_p^2] \Phi_p(\mathbf{r}) = 0, & \mathbf{r} \in \text{ice layer}, \\ [\nabla^2 + k_{sh}^2] \Psi_{sh}(\mathbf{r}) = 0, & \mathbf{r} \in \text{ice layer}, \\ [\nabla^2 + k_{wi}^2] \Phi_{wi}(\mathbf{r}) = 0, & \mathbf{r} \in \text{water}, \\ [\nabla^2 + k_s^2] \Phi_s(\mathbf{r}) = 0, & \mathbf{r} \in \text{sediment}, \end{cases} \quad (1)$$

where $\mathbf{r} = (x, z)$ is the position vector, $k_p = \omega/c_p$ and $k_{sh} = \omega/c_{sh}$ are the ice compressional and shear wavenumbers, respectively, $k_{wi} = \omega/c_{wi}$ is the water wavenumber, and $k_s = \omega/c_s$ is the seabed wavenumber. The boundary conditions at each interface at \mathbf{r}_{bi} can be expressed as

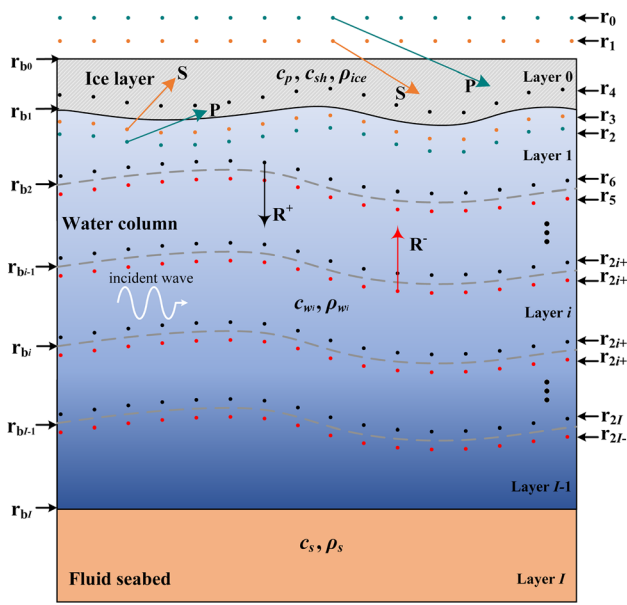


FIG. 1. Schematic of ESM-SUBICE for the range-dependent sound propagation in an ice-covered ocean waveguide with horizontally stratified media. The black circles denote those ESs replacing the reflections by the ice cover and by the adjacent upper fluid layers. The red circles denote those ESs reproducing the reflection by the adjacent lower fluid layer. The green and orange circles represent those ESs generating the compressional and shear potentials in the ice cover, respectively.

$$\begin{cases} \hat{\mathbf{n}} \cdot \boldsymbol{\tau}(\mathbf{r}_{b_0}) \cdot \hat{\mathbf{n}}|_- = 0, & (i=0), \\ \hat{\mathbf{n}} \times [\boldsymbol{\tau}(\mathbf{r}_{b_0}) \cdot \hat{\mathbf{n}}]|_- = 0, & (i=0), \\ \hat{\mathbf{n}} \cdot \boldsymbol{\tau}(\mathbf{r}_{b_i}) \cdot \hat{\mathbf{n}}|_- = -p(\mathbf{r}_{b_i})|_+, & (i=1), \\ \hat{\mathbf{n}} \times [\boldsymbol{\tau}(\mathbf{r}_{b_i}) \cdot \hat{\mathbf{n}}]|_- = 0, & (i=1), \\ \hat{\mathbf{n}} \cdot \mathbf{u}(\mathbf{r}_{b_i})|_- = \hat{\mathbf{n}} \cdot \mathbf{u}(\mathbf{r}_{b_i})|_+, & (1 \leq i \leq I), \\ p(\mathbf{r}_{b_i})|_- = p(\mathbf{r}_{b_i})|_+, & (i=I), \end{cases} \quad (2)$$

where \mathbf{u} is the displacement, $\boldsymbol{\tau}$ is the stress tensor, p is the sound pressure, and $\hat{\mathbf{n}}$ denotes the normal unit vector to the corresponding boundary. The first two equations in Eq. (2) represent the zero traction at the air–ice interface (vanishing normal and tangential stresses), while the remaining refer to the continuity of normal stress across the ice–water interface, zero tangential stress at the ice–water interface, continuity of pressure and normal displacement across the ice–water interface, and each interface between two adjacent fluid layers, respectively. ESM-SUBICE expresses the solution to Eq. (1) as a superposition of basis functions (Green's functions) with their unknown coefficients solved by imposing the boundary conditions defined in Eq. (2). Herein, the scalar and shear potential Green's functions, $G_{\Phi_{p,wi,s}}$ and $G_{\Psi_{sh}}$, satisfy

$$\begin{cases} [\nabla^2 + k_p^2] G^{\Phi_p}(\mathbf{r}, \mathbf{r}') = \delta(\mathbf{r} - \mathbf{r}'), & \mathbf{r} \in \text{ice layer}, \\ [\nabla^2 + k_{sh}^2] G^{\Psi_{sh}}(\mathbf{r}, \mathbf{r}') = \delta(\mathbf{r} - \mathbf{r}'), & \mathbf{r} \in \text{ice layer}, \\ [\nabla^2 + k_{wi}^2] G^{\Phi_{wi}}(\mathbf{r}, \mathbf{r}') = \delta(\mathbf{r} - \mathbf{r}'), & \mathbf{r} \in \text{water}, \\ [\nabla^2 + k_s^2] G^{\Phi_s}(\mathbf{r}, \mathbf{r}') = \delta(\mathbf{r} - \mathbf{r}'), & \mathbf{r} \in \text{seabed}. \end{cases} \quad (3)$$

The first step of ESM-SUBICE is to decompose the waveguide field. In the elastic ice layer, the scalar and shear fields can be separated into the primary and secondary waves (P and S waves) excited by sound (those induced by the sound wave interacting with the ice–water interface) and those reflected by the air–ice interface. The scalar field in the i th water layer consists of the reflections by the $i-1$ th and $i+1$ th layers. Since an infinite, half-space fluid seabed is assumed, the field in the sediment is solely dominated by the water–seabed transmission from the $I-1$ th layer.

After the field decomposition, each separated component of the waveguide field is replaced with a set of equivalent sources (ESs) that are placed either above or below the corresponding boundary, as shown in Fig. 1. For the elastic wave propagation within the ice, two sets of ESs below the ice–water interface are used to replace the sound-generated P and S wave, respectively, one at \mathbf{r}_2 and the other at \mathbf{r}_3 . To reproduce the P and S wave reflections by the air–ice interface, ESs above the air–ice interface at \mathbf{r}_0 and \mathbf{r}_1 are deployed, respectively. Green's function of each elastic wave ES is given by

$$\begin{cases} G^{\Phi_p}(\mathbf{r}, \mathbf{r}') = \frac{j}{4} H_0^{(2)}(k_p |\mathbf{r} - \mathbf{r}'|), \\ G^{\Psi_{sh}}(\mathbf{r}, \mathbf{r}') = \frac{j}{4} H_0^{(2)}(k_{sh} |\mathbf{r} - \mathbf{r}'|), \end{cases} \quad (4)$$

where $\mathbf{r}' = (x', z')$ is the ES position. To reproduce the acoustic propagation in the water column, the i th fluid layer requires two sets of ESs, one above the layer's upper boundary at \mathbf{r}_{2i+2} and the other below its lower boundary at \mathbf{r}_{2i+3} , to replace the reflections by the last and next layers, respectively. If the fluid seabed is range independent, only

one set of ESs above the $I - 1$ th interface at \mathbf{r}_{2I} is required, Green's function of which automatically satisfy the water-seabed boundary condition defined by Eq. (2). By doing this, Green's function of each ES that replaces sound propagation in the i th layer is given by

$$G^{\Phi_{w_i}}(\mathbf{r}, \mathbf{r}') = \begin{cases} \frac{j}{4} H_0^{(2)}(k_{w_i} |\mathbf{r} - \mathbf{r}'|), & (1 \leq i < I - 1), \\ \frac{j}{4} \left[H_0^{(2)}(k_{w_{I-1}} |\mathbf{r} - \mathbf{r}'|) + \sum_{q=0}^Q a_q H_0^{(2)}(k_{w_{I-1}} |\mathbf{r} - \mathbf{r}_q|) \right], & (i = I - 1), \end{cases} \quad (5)$$

where $G^{\Phi_{w_{I-1}}}$ is the half-space water-seabed Green's function, which can be calculated using the complex image method (CIM).^{40,41} The first term of $G^{\Phi_{w_{I-1}}}$ is the direct wave propagation from the source, and the second term represents the water-seabed reflection generated by complex image sources. In the above formula, Q is the order of image source, Q is the total number of image sources, and a_q and \mathbf{r}_q are the amplitude and position of the q th image source. We calculate a_q and α_q through a nonlinear optimization that matches the exponential summation with the plane wave reflection coefficient of seabed using a Levenberg-Marquardt method. Details about the complex image method are referred to in Sec. II B.

After all ES configurations are settled, we, then, write the boundary conditions defined in Eq. (2) in terms of ES amplitudes. Since $G^{\Phi_{w_{I-1}}}$ automatically satisfies the water-seabed boundary condition, the continuity of pressure and normal displacement at \mathbf{r}_{b_I} is omitted, and $2I + 1$ remaining boundary conditions need to be re-written. We start with the derivation of the displacement vector. The displacement vectors in the elastic ice layer and water column are given by

$$\mathbf{u}(\mathbf{r}) = \begin{cases} \frac{1}{\omega^2 \rho_{ice}} [\nabla \Phi_p(\mathbf{r}) + \nabla \times [0, \Psi_{sh}(\mathbf{r}), 0]], & \mathbf{r} \in \text{ice layer}, \\ \frac{1}{\omega^2 \rho_{w_i}} \nabla \Phi_{w_i}(\mathbf{r}), & \mathbf{r} \in \text{water}. \end{cases} \quad (6)$$

In the elastic ice layer, the relation between the stress tensor and the displacement in 2D is given by

$$\begin{cases} \tau_{xx} = (\lambda_{sh} + 2\mu) \frac{\partial \mathbf{u}_x}{\partial x} + \lambda_{sh} \frac{\partial \mathbf{u}_z}{\partial z}, \\ \tau_{xz} = \mu \left(\frac{\partial \mathbf{u}_x}{\partial z} + \frac{\partial \mathbf{u}_z}{\partial x} \right), \\ \tau_{zz} = (\lambda_{sh} + 2\mu) \frac{\partial \mathbf{u}_z}{\partial z} + \lambda_{sh} \frac{\partial \mathbf{u}_x}{\partial x}, \end{cases} \quad (7)$$

where

$$\begin{cases} \mathbf{u}_x = \frac{1}{\omega^2 \rho_{ice}} \left(\frac{\partial \Phi_p}{\partial x} - \frac{\partial \Psi_{sh}}{\partial z} \right), \\ \mathbf{u}_z = \frac{1}{\omega^2 \rho_{ice}} \left(\frac{\partial \Phi_p}{\partial z} + \frac{\partial \Psi_{sh}}{\partial x} \right) \end{cases} \quad (8)$$

while, in the water column, the displacement vector reduces to

$$\begin{cases} \mathbf{u}_x = \frac{1}{\omega^2 \rho_w} \frac{\partial \Phi_{w_i}}{\partial x}, \\ \mathbf{u}_z = \frac{1}{\omega^2 \rho_w} \frac{\partial \Phi_{w_i}}{\partial z}. \end{cases} \quad (9)$$

Next, we rewrite the normal displacement in the ice layer in terms of ES amplitudes,

$$\begin{cases} u_p(\mathbf{r}) = \sum_{n=1}^N G^{u_p}(\mathbf{r}, \mathbf{r}_{0(n)}) s_{0(n)} + \sum_{n=1}^N G^{u_p}(\mathbf{r}, \mathbf{r}_{2(n)}) s_{2(n)}, \\ u_{sh}(\mathbf{r}) = \sum_{n=1}^N G^{u_{sh}}(\mathbf{r}, \mathbf{r}_{1(n)}) s_{1(n)} + \sum_{n=1}^N G^{u_{sh}}(\mathbf{r}, \mathbf{r}_{3(n)}) s_{3(n)}, \end{cases} \quad (10)$$

where the subscript (n) specifies the n th ES of each set, $s_{(n)}$ is its amplitude, N is the total ES number of each set, and u_p and u_{sh} denote the normal components of the compressional and shear displacements, respectively. Similarly, the stress tensor can be re-written as

$$\begin{cases} \tau_{p_{nor}}(\mathbf{r}) = \sum_{n=1}^N G^{\tau_{p_{nor}}}(\mathbf{r}, \mathbf{r}_{0(n)}) s_{0(n)} + \sum_{n=1}^N G^{\tau_{p_{nor}}}(\mathbf{r}, \mathbf{r}_{2(n)}) s_{2(n)}, \\ \tau_{sh_{nor}}(\mathbf{r}) = \sum_{n=1}^N G^{\tau_{sh_{nor}}}(\mathbf{r}, \mathbf{r}_{1(n)}) s_{1(n)} + \sum_{n=1}^N G^{\tau_{sh_{nor}}}(\mathbf{r}, \mathbf{r}_{3(n)}) s_{3(n)}, \\ \tau_{p_{tan}}(\mathbf{r}) = \sum_{n=1}^N G^{\tau_{p_{tan}}}(\mathbf{r}, \mathbf{r}_{0(n)}) s_{0(n)} + \sum_{n=1}^N G^{\tau_{p_{tan}}}(\mathbf{r}, \mathbf{r}_{2(n)}) s_{2(n)}, \\ \tau_{sh_{tan}}(\mathbf{r}) = \sum_{n=1}^N G^{\tau_{sh_{tan}}}(\mathbf{r}, \mathbf{r}_{1(n)}) s_{1(n)} + \sum_{n=1}^N G^{\tau_{sh_{tan}}}(\mathbf{r}, \mathbf{r}_{3(n)}) s_{3(n)}, \end{cases} \quad (11)$$

where $\tau_{p_{nor}}$ and $\tau_{sh_{nor}}$ denote the normal components of the compressional and shear stress tensors, respectively, and $\tau_{p_{tan}}$ and $\tau_{sh_{tan}}$ denote the tangential components of the compressional and shear stress tensors, respectively. According to Eq. (8), the normal-displacement Green's functions, $G^{u_p}(\mathbf{r}, \mathbf{r}')$, and $G^{u_{sh}}(\mathbf{r}, \mathbf{r}')$, have the following mathematical expressions:

$$\begin{cases} G^{u_p}(\mathbf{r}, \mathbf{r}') = \frac{1}{\omega^2 \rho_{ice}} \left[\hat{\mathbf{n}}_x \frac{\partial}{\partial x} + \hat{\mathbf{n}}_z \frac{\partial}{\partial z} \right] G^{\Phi_p}(\mathbf{r}, \mathbf{r}'), \\ G^{u_{sh}}(\mathbf{r}, \mathbf{r}') = \frac{1}{\omega^2 \rho_{ice}} \left[-\hat{\mathbf{n}}_x \frac{\partial}{\partial z} + \hat{\mathbf{n}}_z \frac{\partial}{\partial x} \right] G^{\Psi_{sh}}(\mathbf{r}, \mathbf{r}'), \end{cases} \quad (12)$$

while the normal and tangential components of the stress tensors, $G^{\tau_{p_{nor}}}(\mathbf{r}, \mathbf{r}')$, $G^{\tau_{sh_{nor}}}(\mathbf{r}, \mathbf{r}')$, $G^{\tau_{p_{tan}}}(\mathbf{r}, \mathbf{r}')$, and $G^{\tau_{sh_{tan}}}(\mathbf{r}, \mathbf{r}')$, are given by

$$\begin{cases} G^{\tau_{p_{nor}}}(\mathbf{r}, \mathbf{r}') = \frac{1}{\omega^2 \rho_{ice}} [\hat{\mathbf{n}}_x^2 A_1 + \hat{\mathbf{n}}_z^2 B_1 + 2\hat{\mathbf{n}}_x \hat{\mathbf{n}}_z C_1], \\ G^{\tau_{sh_{nor}}}(\mathbf{r}, \mathbf{r}') = \frac{1}{\omega^2 \rho_{ice}} [\hat{\mathbf{n}}_x^2 A_2 + \hat{\mathbf{n}}_z^2 B_2 + 2\hat{\mathbf{n}}_x \hat{\mathbf{n}}_z C_2], \\ G^{\tau_{p_{tan}}}(\mathbf{r}, \mathbf{r}') = \frac{1}{\omega^2 \rho_{ice}} [(\hat{\mathbf{n}}_x^2 - \hat{\mathbf{n}}_z^2) C_1 + \hat{\mathbf{n}}_z \hat{\mathbf{n}}_x (B_1 - A_1)], \\ G^{\tau_{sh_{tan}}}(\mathbf{r}, \mathbf{r}') = \frac{1}{\omega^2 \rho_{ice}} [(\hat{\mathbf{n}}_x^2 - \hat{\mathbf{n}}_z^2) C_2 + \hat{\mathbf{n}}_z \hat{\mathbf{n}}_x (B_2 - A_2)], \end{cases} \quad (13)$$

where

$$\left\{ \begin{array}{l} A_1 = \left[(\lambda_{sh} + 2\mu) \frac{\partial^2}{\partial x^2} + \lambda_{sh} \frac{\partial^2}{\partial z^2} \right] G^{\Phi_p}(\mathbf{r}, \mathbf{r}'), \\ B_1 = \left[(\lambda_{sh} + 2\mu) \frac{\partial^2}{\partial z^2} + \lambda_{sh} \frac{\partial^2}{\partial x^2} \right] G^{\Phi_p}(\mathbf{r}, \mathbf{r}'), \\ C_1 = 2\mu \frac{\partial^2 G^{\Phi_p}(\mathbf{r}, \mathbf{r}')}{\partial x \partial z}, \\ A_2 = \left[-(\lambda_{sh} + 2\mu) \frac{\partial^2}{\partial x \partial z} + \lambda_{sh} \frac{\partial^2}{\partial z \partial x} \right] G^{\Psi_{sh}}(\mathbf{r}, \mathbf{r}'), \\ B_2 = \left[(\lambda_{sh} + 2\mu) \frac{\partial^2}{\partial z \partial x} - \lambda_{sh} \frac{\partial^2}{\partial x \partial z} \right] G^{\Psi_{sh}}(\mathbf{r}, \mathbf{r}'), \\ C_2 = \mu \left[-\frac{\partial^2}{\partial z^2} + \frac{\partial^2}{\partial x^2} \right] G^{\Psi_{sh}}(\mathbf{r}, \mathbf{r}'), \end{array} \right. \quad (14)$$

and $\hat{\mathbf{n}}_x$ and $\hat{\mathbf{n}}_z$ are the horizontal and vertical components of $\hat{\mathbf{n}}$.

On the other hand, the sound pressure and normal displacement in the water column can be written as

$$\left\{ \begin{array}{l} p_{w_i}(\mathbf{r}) = \sum_{n=1}^N G^{\Phi_{w_i}}(\mathbf{r}, \mathbf{r}_{2i+2(n)}) s_{2i+2(n)} + \sum_{n=1}^N G^{\Phi_{w_i}}(\mathbf{r}, \mathbf{r}_{2i+3(n)}) s_{2i+3(n)}, \quad (1 \leq i < I-1), \\ u_{w_i}(\mathbf{r}) = \sum_{n=1}^N G^{u_{w_i}}(\mathbf{r}, \mathbf{r}_{2i+2(n)}) s_{2i+2(n)} + \sum_{n=1}^N G^{u_{w_i}}(\mathbf{r}, \mathbf{r}_{2i+3(n)}) s_{2i+3(n)}, \quad (1 \leq i < I-1), \\ p_{w_{I-1}}(\mathbf{r}) = \sum_{n=1}^N G^{\Phi_{w_{I-1}}}(\mathbf{r}, \mathbf{r}_{2I(n)}) s_{2I(n)}, \quad (i = I-1), \\ u_{w_{I-1}}(\mathbf{r}) = \sum_{n=1}^N G^{u_{w_{I-1}}}(\mathbf{r}, \mathbf{r}_{2I(n)}) s_{2I(n)}, \quad (i = I-1), \end{array} \right. \quad (15)$$

where u_{w_i} denotes the normal displacement in water with respect to the corresponding boundary, and $G^{u_{w_i}}$ is the normal-displacement Green's function in water with a relation to $G^{\Phi_{w_i}}$ of

$$G^{u_{w_i}}(\mathbf{r}, \mathbf{r}') = \frac{1}{\omega^2 \rho_{w_i}} \left[\hat{\mathbf{n}}_x \frac{\partial}{\partial x} + \hat{\mathbf{n}}_z \frac{\partial}{\partial z} \right] G^{\Phi_{w_i}}(\mathbf{r}, \mathbf{r}'), \quad (1 \leq i \leq I-1). \quad (16)$$

For each interface at r_{b_i} ($i \leq I - 1$), considering a vector of field points $r_{b_i}(1), r_{b_i}(2), \dots, r_{b_i}(N)$ and, after substituting for the boundary conditions given in Eq. (2) in terms of the ES amplitudes given by Eqs. (10), (11) and (15), this yields a linear system coupling all fields generated by $2I + 1$ sets of ES,

$$\begin{aligned}
& \mathbf{G}_{0,0}^{\tau_{pnor}} \quad \mathbf{G}_{0,1}^{\tau_{shnor}} \quad \mathbf{G}_{0,2}^{\tau_{pnor}} \quad \mathbf{G}_{0,3}^{\tau_{shnor}} \\
& \mathbf{G}_{0,0}^{\tau_p \tan} \quad \mathbf{G}_{0,1}^{\tau_{sh} \tan} \quad \mathbf{G}_{0,2}^{\tau_p \tan} \quad \mathbf{G}_{0,3}^{\tau_{sh} \tan} \\
& \mathbf{G}_{1,0}^{\tau_p \tan} \quad \mathbf{G}_{1,1}^{\tau_{sh} \tan} \quad \mathbf{G}_{1,2}^{\tau_p \tan} \quad \mathbf{G}_{1,3}^{\tau_{sh} \tan} \\
& \mathbf{G}_{1,0}^{\tau_{pnor}} \quad \mathbf{G}_{1,1}^{\tau_{shnor}} \quad \mathbf{G}_{1,2}^{\tau_{pnor}} \quad \mathbf{G}_{1,3}^{\tau_{shnor}} \quad \mathbf{G}_{1,4}^{\Phi_{w_1}} \quad \mathbf{G}_{1,5}^{\Phi_{w_1}} \\
& -\mathbf{G}_{1,0}^{u_p} \quad -\mathbf{G}_{1,1}^{u_{sh}} \quad -\mathbf{G}_{1,2}^{u_p} \quad -\mathbf{G}_{1,3}^{u_{sh}} \quad \mathbf{G}_{1,4}^{u_{w_1}} \quad \mathbf{G}_{1,5}^{u_{w_1}} \\
& \dots \quad \dots \quad \dots \quad \dots \quad \dots \quad \dots \\
& \mathbf{G}_{i,2i+2}^{\Phi_{w_i}} \quad \mathbf{G}_{i,2i+3}^{\Phi_{w_i}} \quad -\mathbf{G}_{i,2i+4}^{\Phi_{w_{i+1}}} \quad -\mathbf{G}_{i,2i+5}^{\Phi_{w_{i+1}}} \\
& \mathbf{G}_{i,2i+2}^{u_{w_i}} \quad \mathbf{G}_{i,2i+3}^{u_{w_i}} \quad -\mathbf{G}_{i,2i+4}^{u_{w_{i+1}}} \quad -\mathbf{G}_{i,2i+5}^{u_{w_{i+1}}} \\
& \dots \quad \dots \quad \dots \quad \dots \quad \dots \quad \dots \\
& \mathbf{G}_{I-1,2I-2}^{\Phi_{w_{I-2}}} \quad \mathbf{G}_{I-1,2I-1}^{\Phi_{w_{I-2}}} \quad -\mathbf{G}_{I-1,2I}^{\Phi_{w_{I-1}}} \\
& \mathbf{G}_{I-1,2I-2}^{u_{w_{I-2}}} \quad \mathbf{G}_{I-1,2I-1}^{u_{w_{I-2}}} \quad -\mathbf{G}_{I-1,2I}^{u_{w_{I-1}}} \\
\end{aligned} \tag{20}$$

In the above equations, the entries of the $N \times N$ transfer matrices are calculated using Eqs. (4), (5), (12), (13), and (16), and the subscript i,l of each transfer matrix specifies the boundary field at \mathbf{r}_{b_i} produced by ES placed at \mathbf{r}_l , i.e.,

$$\mathbf{G}_{i,l} = \mathbf{G}(\mathbf{r}_{b_i}, \mathbf{r}_l). \quad (21)$$

For the source producing the incident field in the first water layer, $\{\mathbf{e}\}$ has the following explicit expression:

$$\{\mathbf{e}\} = \{\mathbf{0}, \mathbf{0}, \mathbf{0}, \mathbf{p}_{inc}(\mathbf{r}_{b_1}), \mathbf{u}_{inc}(\mathbf{r}_{b_1}), -\mathbf{p}_{inc}(\mathbf{r}_{b_2}), -\mathbf{u}_{inc}(\mathbf{r}_{b_2}), \underbrace{\mathbf{0}, \dots, \mathbf{0}}_{(2I-6) \times 0}\}^T, \quad (22)$$

where \mathbf{p}_{inc} and \mathbf{u}_{inc} are the $1 \times N$ vectors of incident pressures and normal displacements at the corresponding boundary, respectively. For the source in the i th layer ($i < I$ because the source is generally deployed in water in most of situations), $\{\mathbf{e}\}$ is given by

$$\{\mathbf{e}\} = \{\underbrace{\mathbf{0}, \dots, \mathbf{0}}_{(2i-1) \times 0}, \mathbf{p}_{inc}(\mathbf{r}_{b_i}), \mathbf{u}_{inc}(\mathbf{r}_{b_i}), -\mathbf{p}_{inc}(\mathbf{r}_{b_{i+1}}), -\mathbf{u}_{inc}(\mathbf{r}_{b_{i+1}}), \underbrace{\mathbf{0}, \dots, \mathbf{0}}_{(2I-2i-2) \times 0}\}^T. \quad (23)$$

When a monopole point source of unit amplitude is considered, the incident field quantities are determined by Green's function multiplied by 4π . The water-seabed Green's function or the free-field one is used depending on which layer the source is in. If the source is placed at the i th layer ($i < I-1$), the free-field Green's function is used to evaluate \mathbf{p}_{inc} and \mathbf{u}_{inc} at the upper and lower interfaces of the layer. This gives the RHS of Eq. (16) such that the boundary conditions across each interface in the waveguide are rigorously enforced. When the source is in the $I-1$ th layer, \mathbf{p}_{inc} and \mathbf{u}_{inc} should account for the seabed reflection. This is because the global coupling matrix is assembled using the water-seabed Green's function that automatically enforces the boundary conditions of a range-independent seabed. In this case, \mathbf{p}_{inc} and \mathbf{u}_{inc} must be evaluated using the CIM described in this article. After solving the linear system given by Eq. (17), the waveguide field in the ice and water can be calculated forwardly using Eqs. (10), (11), and (15). See Fig. 2 for the flow chart of the algorithm in ESM-SUBICE.

In addition, ESM-SUBICE can handle the range-dependent fluid seabed similarly to dealing with the multiple water layer by arranging two sets of ESs above and below the water-seabed interface. This is based on the fact that: (a) Green's functions are the basis functions of the solution to the Helmholtz equation, and (b) the boundary conditions across the interface between two fluid layers are strictly enforced by imposing Eq. (2). By doing this, Green's function of the ESs above the $I-1$ th layer should be the free-field one but with the seabed wave-number k_s , such that the $I-1$ th layer can then be treated as an infinite seabed without the lower boundary. When dealing with a range-dependent elastic seabed, an additional set of ESs above the seabed boundary is required to produce the shear wave in the seabed. The corresponding procedure for assembling the global coupling matrix is similar to that in the fluid seabed situation but with an additional fluid-solid boundary condition imposed at the seabed interface. Since the seabed elasticity is out of the scope of the present analysis, we only

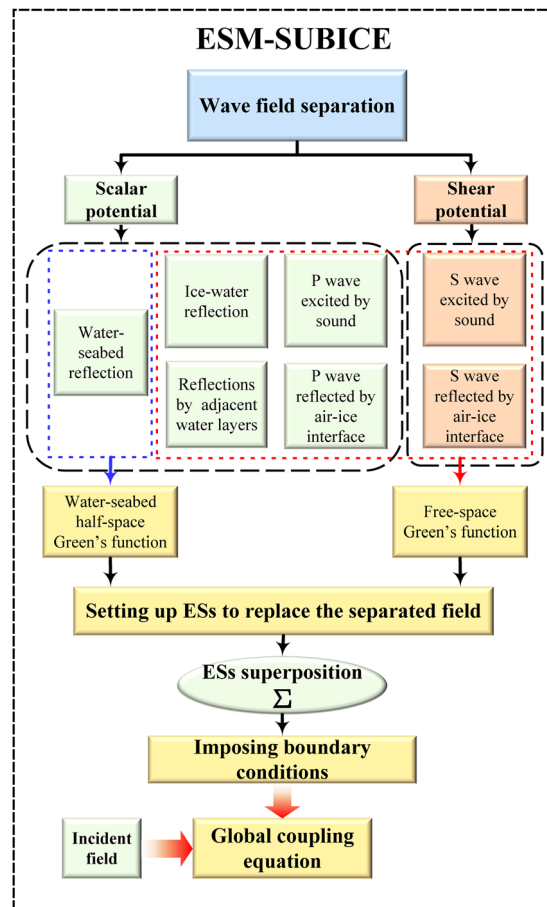


FIG. 2. Flowcharts summarizing the algorithm involved in ESM-SUBICE.

explain how to address a range-dependent elastic seabed theoretically without going into depth with it further.

B. Complex image method for evaluating the water-seabed half space Green's function

For the last set of ESs, Green's function for a half-space with two homogeneous layers is required. The method of complex images⁴⁰ is employed to calculate such a half-space Green's function. The advantage of the CIM is that the amplitudes and complex positions of images only need to determine one time, and Green's function for arbitrary frequencies can be obtained with simple modifications on the image configurations.⁴¹ In addition, CIM solutions converge fast using only a few orders of images, which is numerically efficient.

Here, we consider a two-layer half-space shown in Fig. 3. The water-seabed interface is allowed to be sloped with a slope angle θ . A new coordinate system (x_θ, z_θ) is introduced by rotating the original coordinate (x, z) by θ , where

$$\begin{cases} x_\theta = \frac{x}{\cos \theta} + (z - x \tan \theta) \sin \theta, \\ z_\theta = (z - x \tan \theta) \cos \theta \end{cases} \quad (24)$$

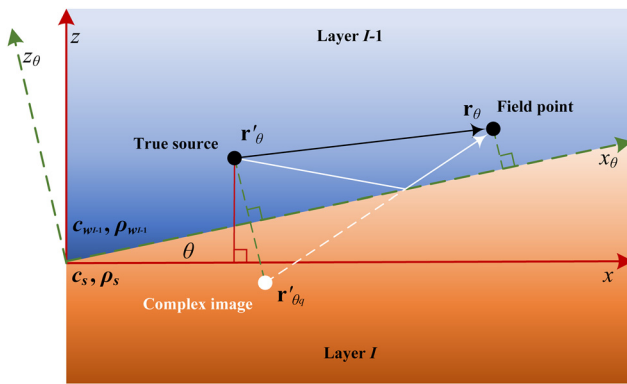


FIG. 3. Schematic of the complex image method in a rotated coordinate system for evaluating the water-seabed Green's function.

with the water-seabed interface placed at $z' = 0$. The water-seabed Green's function for a field point $\mathbf{r}_\theta = (x_\theta, z_\theta)$ due to a source at $\mathbf{r}_\theta' = (x'_\theta, z'_\theta)$ above the half-space can be represented as the wavenumber integral expression, which is as follows:

$$G(\mathbf{r}_\theta, \mathbf{r}'_\theta) = \frac{j}{4} H_0^{(2)}(k_{w_{l-1}} |\mathbf{r}_\theta - \mathbf{r}'_\theta|) + \frac{1}{\pi} \int_0^\infty R(h) \frac{e^{-j\gamma_1(z_\theta + z'_\theta)}}{2j\gamma_1} \cos(h|x_\theta - x'_\theta|) dh, \quad (25)$$

where h is the horizontal wavenumber, $\gamma_1(h) = \sqrt{(k_{w_{l-1}}^2 - h^2)}$ is the vertical wavenumber in water, and $R(h)$ is the plane-wave reflection coefficient of the water-seabed interface given by

$$R(h) = \frac{\rho_s \Gamma(h) \gamma_1(h) - \rho_{w_{l-1}} \gamma_s(h)}{\rho_s \Gamma(h) \gamma_1(h) + \rho_{w_{l-1}} \gamma_s(h)}, \quad (26)$$

where $\gamma_s(h) = \sqrt{(k_s^2 - h^2)}$ is the vertical wavenumber in the seabed, and $\Gamma(h) \equiv 1$ for a fluid seabed. For an elastic seabed, the detailed expression of $\Gamma(h)$ can be found in the existing literature^{17,40} and is not given here to save space.

The integral in Eq. (25) represents the reflected field above the upper half-space. We now write a line source field in terms of the wavenumber integral expression, which is as follows:

$$\frac{j}{4} H_0^{(2)}(k_{w_{l-1}} |\mathbf{r}_\theta - \mathbf{r}'_\theta|) = \frac{1}{\pi} \int_0^\infty \frac{e^{-j\gamma_1(z_\theta - z'_\theta)}}{2j\gamma_1} \cos(h|x_\theta - x'_\theta|) dh, \quad (27)$$

and assume a complex image depth $z'_{\theta_q} = -z'_\theta + j\alpha_q$. The field generated by Q such line sources is as follows:

$$\sum_{q=0}^Q a_q \frac{j}{4} H_0^{(2)}(k_{w_{l-1}} |\mathbf{r}_\theta - \mathbf{r}'_{\theta_q}|) = \frac{1}{\pi} \int_0^\infty \left[\sum_{q=0}^Q a_q e^{j\gamma_1 z'_{\theta_q}} \right] \frac{e^{-j\gamma_1(z_\theta + z'_\theta)}}{2j\gamma_1} \cos(h|x_\theta - x'_\theta|) dh. \quad (28)$$

If the parameters a_q and α_q are determined by

$$\sum_{q=0}^Q a_q e^{j\gamma_1(h)\alpha_q} \approx R(h), \quad (29)$$

the reflected field in Eq. (25), then, can be replaced by

$$G_r(\mathbf{r}_\theta, \mathbf{r}'_\theta) = \sum_{q=0}^Q a_q \frac{j}{4} H_0^{(2)}(k_{w_{l-1}} |\mathbf{r}_\theta - \mathbf{r}'_{\theta_q}|), \quad (30)$$

where \mathbf{r}'_{θ_q} is the position vector of the complex image and $|\mathbf{r}_\theta - \mathbf{r}'_{\theta_q}| = \sqrt{(x_\theta - x'_{\theta_q})^2 + (z_\theta + z'_{\theta_q} - i\alpha_q)^2}$. The exponential fit can be solved by a Levenberg–Marquardt method based on Eq. (29). In order to correct the singular behavior of the Green's function, the asymptotic term with the singularity in the $R(h)$ should be removed while performing the exponential fit. For a fluid seabed, only one asymptotic term $R_\infty = (\rho_s - \rho_{w_{l-1}})/(\rho_s + \rho_{w_{l-1}})$ should be subtracted.

Once the amplitudes and complex positions of images are determined, the half-space Green's function can be calculated using Eq. (5), with $a_0 = R_\infty$ and $\alpha_0 = 0$. Generally, five exponentials are sufficient to fit the reflection coefficient of fluid seabed.⁴⁰ Therefore, five exponentials are used to calculate the half-space Green's function in this paper.

C. Fourier synthesis technique for generating time-domain solutions

The time-domain solution is obtained by a Fourier synthesis technique,^{42,43} in which the frequency-domain solutions over a broadband are first calculated and then transformed into the time domain using the inverse fast Fourier transform,

$$\Phi(x, z, t) = \int_{-\infty}^{+\infty} S(\omega) \Phi(x, z, \omega) e^{-j\omega t} d\omega, \quad (31)$$

where $S(\omega)$ is the source spectrum, and $\Phi(x, z, \omega)$ is the frequency-domain solution calculated by ESM-SUBICE. The above transform is implemented numerically using *ifft* in MATLAB. Note that only the frequency-domain solutions within the broadband of interest need to be computed, outside which zero padding is required before performing *ifft*. In addition, a Tukey window is used as the weighting function in the frequency domain, giving well-defined pulse response in the time domain. The frequency sampling interval is selected as $\Delta f = c_w/2L$ to avoid aliasing,^{42,43} where L is the total propagation range.

III. NUMERICAL SIMULATIONS

This section presents the results of the numerical simulations. First, sound propagation in an iso-velocity ocean with a rough ice layer and a flat fluid seabed is considered. ESM-SUBICE is, then, benchmarked against an FE model, and the significance of ice elasticity is discussed by comparing the TLs predicted by the elastic, fluid, and free-surface ice representations in different ocean environments. Next, sound propagation in more complex stratified ice-covered ocean environments is considered to further examine the effect of the sound-speed profile (SSP) and range dependency on the applicability of effective ice representations. Wavenumber-spectrum analyses are presented to interpret the effect of ice elasticity on propagation and scattering from the modal perspective. Finally, pulse propagation is examined to visualize the effect of scattering from the rough ice-water interface.

To implement ESM-SUBICE, each set of ESs is placed at a conformal line offset from the corresponding boundary by the same

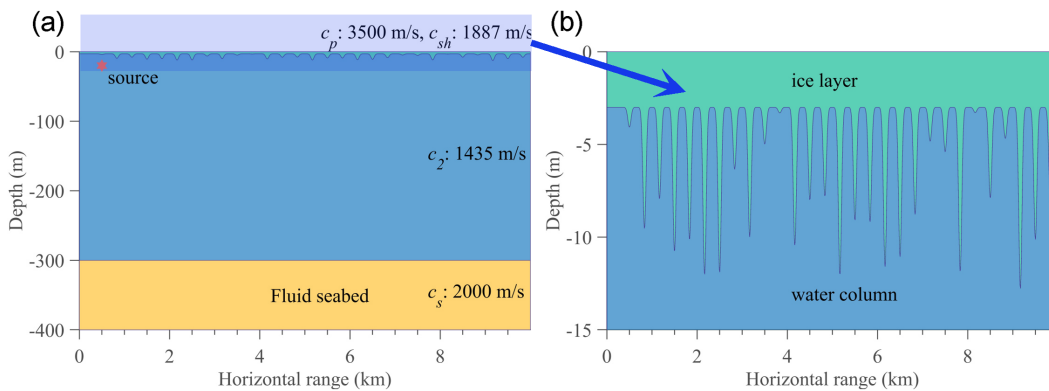


FIG. 4. Setup of the sub-ice ocean environment (a), and a zoomed-in view showing the details of the rough ice–water interface (b).

stand-off distance. The ESs are distributed along these conformal lines with a distance Δ between two adjacent sources of $\lambda/6$ (Refs. 37–39) and a stand-off distance d_s of 2Δ (where λ represents the acoustic wavelength).⁴⁴ A detailed investigation into the selection of the ES configuration in the current study suggested that it provides a reasonable compromise; therefore, this was used in all of the subsequent numerical experiments.

The FE model is implemented using the commercial COMSOL Multiphysics software, with the acoustic–solid interaction model used to couple the sound wave from the water into the solid ice. The FE computational domain is truncated by perfectly matched layer (PML) to absorb the out-going waves at $z = -\infty$ and at $x = \pm\infty$. Triangular meshes with a maximum element size of $\lambda/6$ are used to discretize the computational domain. The fluid–solid coupling boundary is refined automatically, giving a detailed description of the elastic wave field within the ice. PML is composed of a mapping mesh of 20 layers with a thickness of 50 m in each simulation. Such a meshing scheme guarantees a convergent FE solution.^{37–39,43} The FE frequency-domain solver is used to calculate the wave field. The simulations reported throughout this article were implemented using the MATLAB platform (The MathWorks, Inc., Natick, MA) installed on a computer with an Intel Core i9-13900K CPU and 128 GB RAM (Intel, Santa Clara, CA).

A. 2D propagation in an ice-covered, iso-velocity ocean waveguide

The first environment considered is an ice-covered, iso-velocity ocean waveguide with a flat fluid seabed. The compressional- and shear-wave speeds of the ice layer are 3500 and 1888 m/s with the corresponding attenuation coefficients of 0.5 and 1.5 dB/ λ , respectively, and the ice density is 900 kg/m³. The water is of 300-m depth, with a sound speed of 1435 m/s and a density of 1000 kg/m³. The range-independent fluid seabed has a sound speed of 2000 m/s with an attenuation coefficient of 0.2 dB/ λ and a density of 2200 kg/m³. A monopole point source of unit amplitude is considered, and this is placed at (500, -20 m). The computational domain extends from $x = 0$ m to $x = 10$ km and from $z = 0$ m to $z = -300$ m. Note that the FEM requires 100 m deeper space to properly truncate the infinite fluid seabed. The above simulation parameters are used unless otherwise specified.

1. Benchmark example

The first benchmark example is sound propagation under an ice layer with keels. The source frequency is 100 Hz. Figure 4 illustrates the sub-ice ocean environment; the right-hand panel shows a zoomed area plotting the rough ice–water interface. Note that the acoustic wavelength is 15 m, which is comparable with the ice-keel size; therefore, considerable rough scattering is expected in this case. Excellent agreement with the FE model can be seen in Fig. 5, where the TL is plotted as a function of the range with a receiver depth of $z = -200$ m, thus validating that ESM-SUBICE accounts well for the scattering effects of a rough ice–water interface.

2. Propagation of acoustic and elastic waves

Next, we consider wave propagation in the ice-covered ocean waveguide described in Fig. 4. Figure 6(b) gives the sub-ice acoustic propagation under the rough elastic ice layer. For comparison, the results for 3-m-thick ice cover are also given in Fig. 6(a). Visible scattering effects from the rough ice–water interface can be observed in

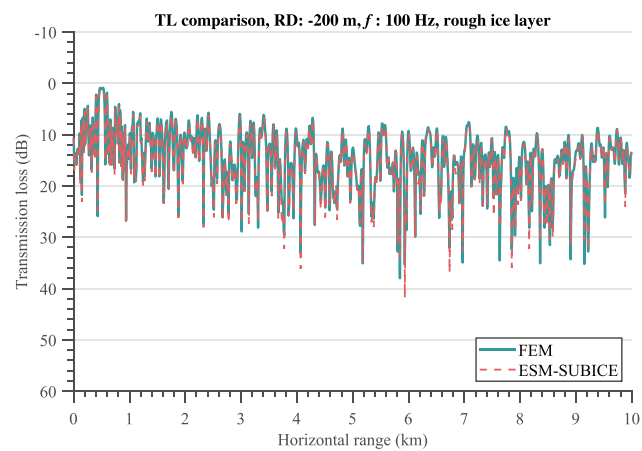


FIG. 5. Transmission loss (TL) as a function of range at 100 Hz, with a receiver and source depth of -20 m. The solid green and dashed red lines correspond to the FEM and ESM-SUBICE results, respectively.

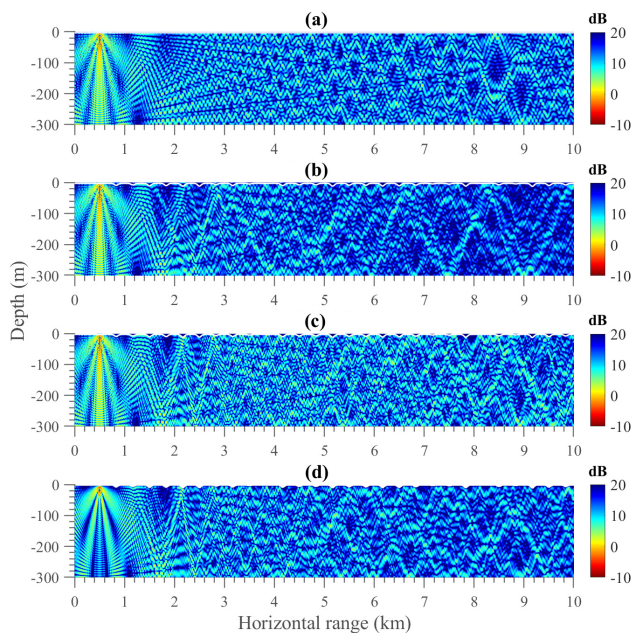


FIG. 6. Sub-ice acoustic-wave propagation (compressional potential) from 0 to 10 km at 100 Hz. The results are given for: (a) 3-m-thick elastic ice, (b) rough elastic ice, (c) fluid ice, and (d) free-surface ice.

Fig. 6(b), and this is associated with greater TLs when compared with Fig. 6(a). The ice keels scatter considerable energy in the direction along which sound penetrates the seabed at supercritical grazing angles. In addition, the roughness of the ice–water interface increases the local grazing angle of the incident waves, promoting water–ice energy transmission. Therefore, more energy is taken out of the system by shear-wave attenuation from compressional-to-shear wave conversion in the rough case. These two mechanisms causes greater TLs at long ranges than in the flat-ice case.

To emphasize the effect of ice elasticity on scattering and propagation, Figs. 6(c) and 6(d) show the results when the ice cover is modeled as a fluid and a free surface, respectively. By comparing Figs. 6(b)–6(d), one can observe that the fluid and free-surface representations overpredict the acoustic energy at long ranges and fail to capture the detailed modal interference pattern presented in Fig. 6(b). This discrepancy is explained by acoustic-elastic coupling, which is not captured in either the fluid or free-surface representations. Furthermore, the free-surface representation fails to capture the elastic waves within the ice, which reflect at the air–ice interface and transmit back into the water column at steep grazing angles with respect to the horizontal. The associated energy is likely to be attenuated in the sediment by the supercritical incidence. This scattering of ice-borne waves is absent in the free-surface representation.

Figure 7 shows zoomed-in areas (above $z = -10$ m) of the compressional wave propagation within the ice cover plotted in Fig. 6. Here, we omit the result from the free-surface representation since waves within the ice are not captured. For the elastic representation, P-wave propagation exhibits observable reflection from the air–ice interface, at which a physically accurate zero-traction boundary is applied. P waves do not vanish near the air–ice interface, and

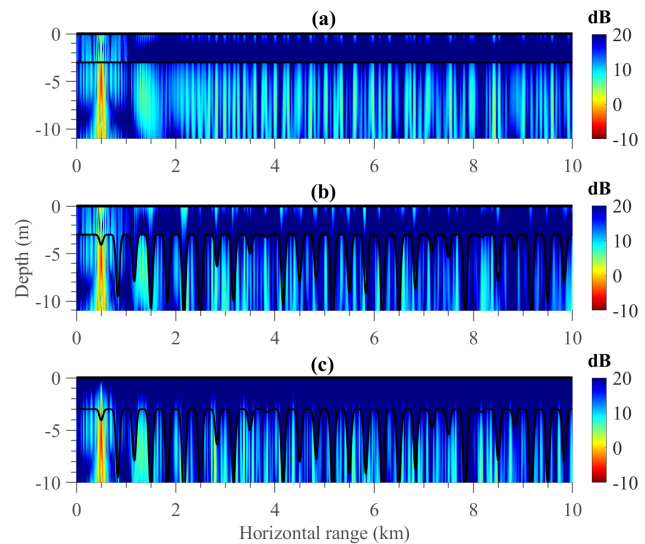


FIG. 7. Compressional wave propagation from $z = 0$ to -10 m and from $x = 0$ to 10 km at 100 Hz for: (a) 3-m-thick elastic ice, (b) rough elastic ice, and (c) fluid ice.

elastic-mode nulls are observed near the ice–water interface. However, the fluid ice representation gives false fields within the ice, exhibiting the impact of pressure release rather than the zero-traction boundary. The field within the fluid ice is almost negligible compared with the P-wave distribution in the elastic ice, indicating that the lack of acoustic-elastic coupling in the fluid representation causes the overprediction of acoustic energy in the ocean. Comparing Figs. 7(a) and 7(b), it can be seen that more energy is transmitted into the rough ice cover than the flat ice, and significant energy transmission occurs in thick ice regions, which coincides with the above analysis.

Figure 8 displays shear-wave propagation within the ice in the flat and rough elastic cases. The S waves exhibit a rather uniform mode shape, with larger amplitudes than P waves due to the consistent compressional-to-shear energy conversion occurring when the acoustic waves interact with the ice. Therefore, S waves are also strong where considerable water–ice transmission occurs. As the propagation range increases, leaky-elastic-wave behaviors are associated with decreasing ice thickness, carrying the energy back into the water column with steeper grazing angles toward the seabed. This also increases the TL, as the re-radiated energy tends to leak into the seabed at supercritical grazing angles. Leaky elastic waves may explain why the S-wave energy is lower in the rough-ice case, even if its average thickness is greater.

To further consider under what conditions the fluid and free-surface representations can provide acceptable predictions, we now compare their depth-averaged TLs in various ocean environments. We first consider different water depths, as shown in Figs. 9(a)–9(c). As the water depth increases, discrepancies among different ice representations become small, with their maxima exceeding 10 dB for a depth of 50 m and their minima within 5 dB when the depth is 300 m. Only low-order modes are supported in shallow water, propagating at shallow grazing angles at long ranges. Due to scattering from elastic ice keels, energy from low-order modes changes its propagation angle from shallow to steep, tending to be transferred to higher-order modes and the plate flexural modes of the ice layer. Since higher-order modes

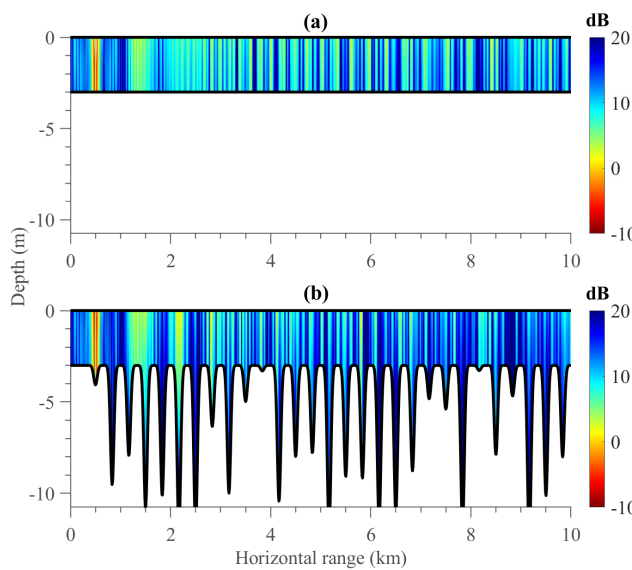


FIG. 8. Shear-wave propagation from $z = 0$ to -10 and from $x = 0$ to 10 km at 100 Hz for: (a) 3-m-thick elastic ice and (b) rough elastic ice.

are cut off in shallow oceans, and the plate flexural modes mainly contribute to the field within the ice, low-order modes gradually become evanescent due to scattering. However, higher-order modes propagating at steep angles are present in deeper oceans, coupling with re-radiation from within the elastic ice layer with steep angles relative to the horizontal. This coupling effect associated with the scattering of

ice-borne waves prevents bottom losses. It is, therefore, reasonable to infer that the fluid and free-surface representations may be acceptable for deep-water environments.

Figures 9(d)–9(f) show the depth-averaged TLs for different ice representations in a 300-m-deep ocean overlying three types of seabed. Significant discrepancies are associated with hard seabeds, which support propagation of higher modes at steep grazing angles relative to the horizontal. This means that those modes also interact with the elastic ice at large grazing angles. Therefore, the harder the seabed, the more energy is transmitted into the ice and then attenuated through compressional-to-shear conversion. We, thus, infer that the fluid and free-surface representations may be acceptable for ocean overlying a soft seabed.

B. 2D propagation in a stratified ice-covered ocean waveguide

We now test ESM-SUBICE for wave propagation in stratified ice-covered ocean waveguides close to realistic and complex Arctic Ocean acoustic environments. We first consider 1200-m-deep water overlying a flat seabed with a depth-dependent sound-speed structure. As shown in Fig. 10(a), the water column is divided into five layers to accommodate sound-speed inhomogeneities, with the top four layers forming a thermocline. The thicknesses of these layers are 25, 25, 50, and 50 m, respectively. The bottom water layer represents the isothermal layer, in which the sound speed barely varies with depth. The sound speeds in these water layers are 1435, 1440, 1445, 1453, and 1460 m/s from the top to bottom. We choose a soft fluid seabed with a sound speed of 1500 m/s, an attenuation coefficient of 0.2 dB, and a density of 1500 kg/m^3 , avoiding ice–water scattering and the impact of

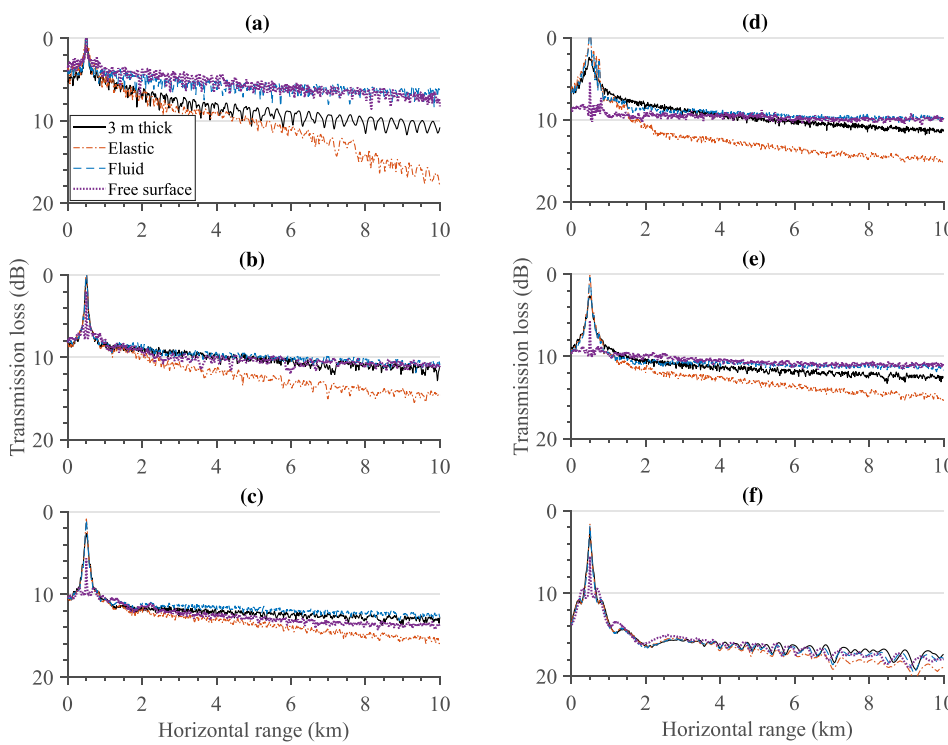


FIG. 9. Depth-averaged TLs for the elastic (solid red lines), fluid (dashed blue lines), and free-surface (dash-dotted purple lines) ice representations in various ocean environments. The left-hand panels show the results in ice-covered oceans with water depths of: (a) 50 m, (b) 150 m, and (c) 300 m. The right-hand panels show the results in ice-covered, 300-m-deep oceans overlying (d) basalt, (e) limestone, and (f) clay seabeds.

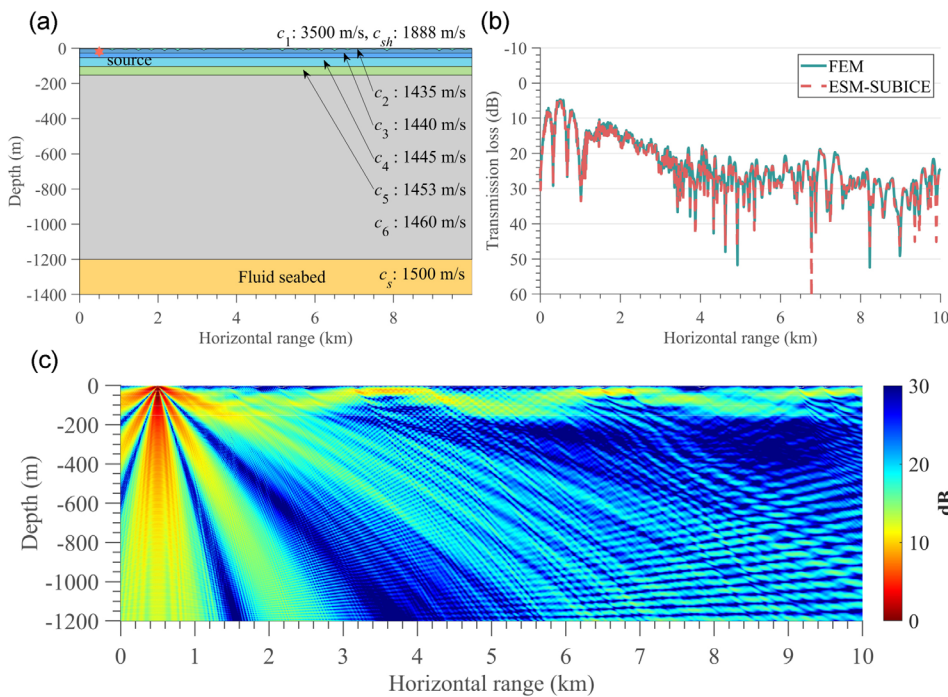


FIG. 10. (a) Setup of the 1200-m-deep, sub-ice ocean environment. (b) The TL as a function of range at 100 Hz with a receiver depth of -200 m and a source depth of -20 m. The solid green and dashed red lines correspond to the FEM and ESM-SUBICE results, respectively. (c) Sub-ice acoustic-wave propagation in 1200-m-deep, up-refractive water covered by rough ice (as in Fig. 4).

up-refraction being overshadowed by seabed reflection. A source with a frequency of 100 Hz is placed at $(500, -20$ m). The same ice material is assumed here as previously described. The computational domain extends from $x = 0$ m to $x = 10$ km and from $z = 0$ m to $z = -1200$ m.

1. Stratified ice-covered ocean waveguide with a flat fluid seabed

A benchmark is first established for ESM-SUBICE through TL comparisons with the FEM at -200 m depth, and the corresponding results are shown in Fig. 10(b). Excellent agreement with the FEM (right-hand panel) validates ESM-SUBICE. Figure 10(c), then, displays the acoustic-wave propagation in the region from $z = 0$ to -1200 m and from $x = 0$ to 10 km. One can observe the apparent up-refraction

caused by the positive sound-speed gradient, bending the acoustic ray reflected by the ice layer back and consequently creating a surface duct above $z = -150$ m. This surface duct intensifies the interaction of the acoustic wave with the elastic ice layer, increasing the grazing angle with respect to the local ice-water interface. Therefore, enhanced water-ice energy transmission is expected from up-refraction.

Although the analysis in Sec. III A 2 suggests that the effective ice representations may be sufficient for a deep-water environment with a soft seabed, the surface duct created by up-refraction can still induce waveguide effects, potentially invalidating these representations by intensifying interactions with the elastic ice. Figure 11 displays TLs for different ice representations with and without the up-refractive SSP at a receiver depth of -20 m. In the presence of the SSP, there is a pronounced waveguide impact with rapid peak-trough shifts with range.

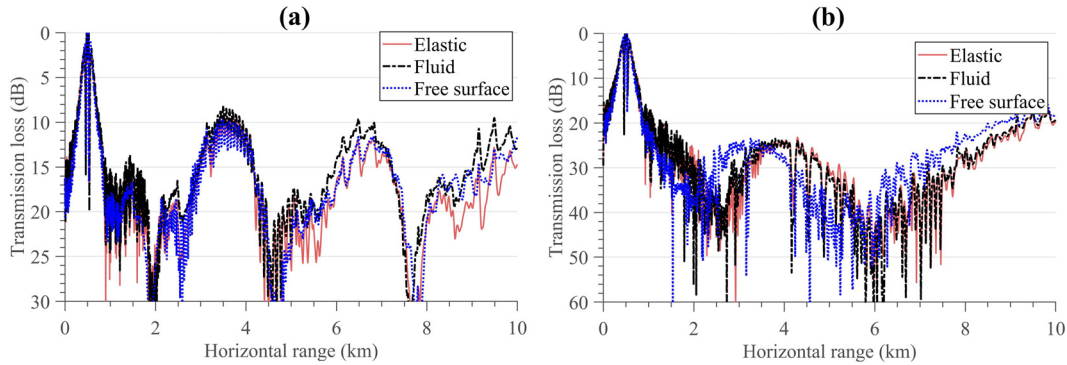


FIG. 11. TL as a function of range at 100 Hz with a receiver and source depth of -20 m. The solid red, dashed blue, and dash-dotted black lines correspond to the results for the elastic, fluid, and free-surface representations, respectively. The left and right panels give the results with and without the up-refractive SSP, respectively.

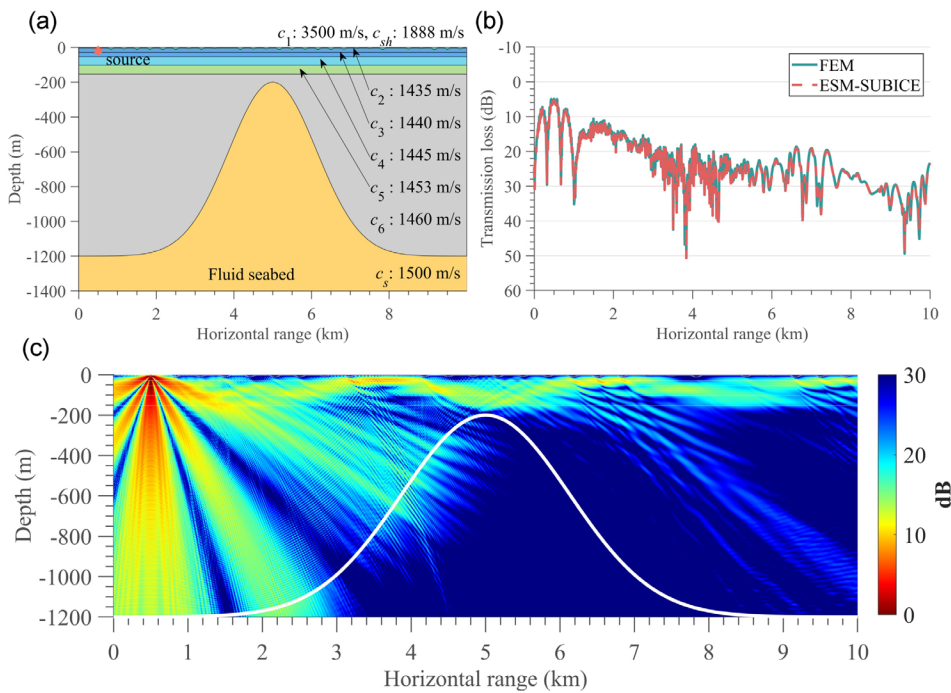


FIG. 12. (a) Setup of the ice-covered seamount. (b) TL as a function of the range at 100 Hz with a receiver depth of -50 m and a source depth of -20 m . The solid green and dashed red lines correspond to the FEM and ESM-SUBICE results, respectively. (c) Sub-ice acoustic-wave propagation in 1200-m-deep up-refractive water overlying a Gaussian seamount.

The fluid representation produces a similar interference pattern to the elastic representation, which is dominated by rough scattering. However, compared with the elastic representation, the specific peak and trough positions shift, and the TL is around 5 dB lower. This is explained by the enhanced acoustic-wave interactions with the elastic ice due to surface ducting. The free-surface ice representation predicts the correct level but fails to capture the detailed interference pattern. Conversely, TLs for the elastic and fluid representations are almost identical in the iso-velocity deep water. This is because steep reflections from within the elastic ice couple into higher-order modes and propagate in deep water (see Sec. III A 2). These results indicate that once the water is strongly up-refractive, the effective ice representations are insufficient, and elasticity should be considered in any sub-ice propagation model to predict accurate TLs.

2. Stratified ice-covered ocean waveguide with a fluid Gaussian seamount

We now consider the same up-refractive deep water overlying a fluid Gaussian seamount. The seabed topography is determined by $z_b(x) = h_0 - h_1 e^{-(x-5000)^2/\delta^2}$, where $h_0 = -1200 \text{ m}$, $h_1 = -1000 \text{ m}$, and $\delta = 1600$. Other simulation parameters remain the same as previously. Again, ESM-SUBICE is validated by a comparison of TL with FEM [Fig. 12(b)]. Figure 12(c) gives the corresponding acoustic-wave propagation, in which the modal cutoff associated with the up-slope propagation can be seen. The modal cutoff induces greater TLs from $x = 6$ to 10 km. However, the surface duct preserves most of the propagation energy by trapping the sound waves within it and thus reducing interactions with the seabed. Interestingly, observable ice-layer scattering patterns (caustics) can be found from 6 to 10 km, over which the seamount shadows the sound. This pattern is absent in the

same region in Fig. 10(c), as the seabed reflection overshadows the ice-layer scattering.

Next, we compare TLs for different ice representations in the Gaussian-seamount case. Figure 13 shows the discrepancies between the elastic and fluid representations, which are slightly larger than those for the flat-seabed case. This is because high-order modes couple with the steep reflections from within the elastic ice. This part of the energy transmits into the sediment and finally decays due to the modal cutoff associated with decreasing water depth. The fluid representation fails to capture the coupling of the high-order modes with the steep re-

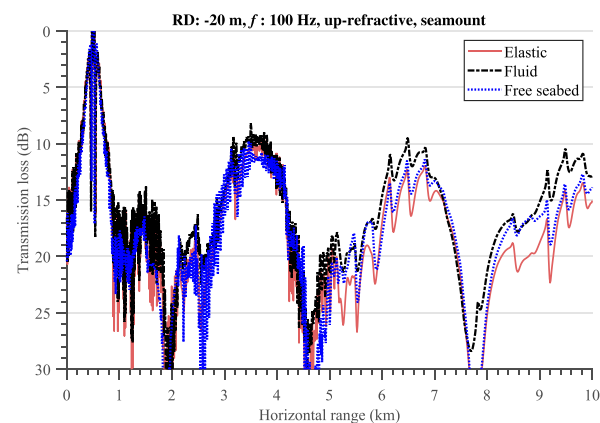


FIG. 13. TL as a function of range at 100 Hz in the Gaussian-seamount case, with a receiver and source depth of -20 m . The solid red, dashed blue, and dash-dotted black lines correspond to the results for the elastic, fluid, and free-surface representations, respectively.

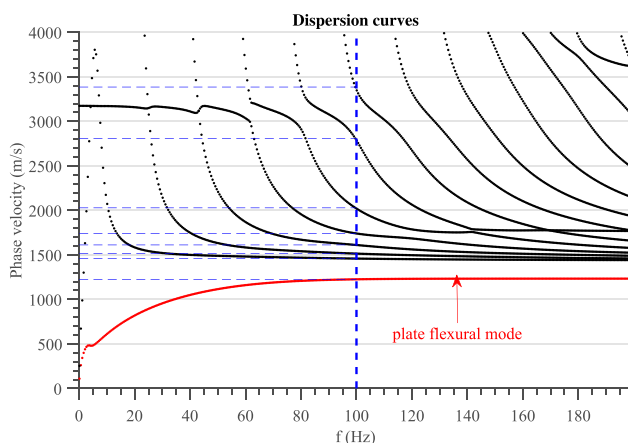


FIG. 14. Dispersion curves calculated by SBFEM for the 50 m-deep waveguide covered by a 10 m-thick ice layer. Other parameters are the same as those in Sec. III A 1.

radiation from the elastic ice and so further overpredicts the acoustic energy at long ranges. This suggests that the coupling is complicated when strong seabed-range dependency is involved, requiring the ice to be treated as an elastic medium.

C. Modal interpretation of the effect of ice elasticity on propagation and scattering

We now interpret the effect of ice elasticity on propagation and scattering from the modal perspective. To do so, the wavenumber-domain spectra are calculated by performing the inverse Fourier transform to the 2D sound pressure output from ESM-SUBICE and normalized by the maximum spectrum amplitude. Waveguide modes are, then, identified by comparing the result with the modal phase velocity computed by a scaled boundary finite element method (SBFEM).⁴⁵ Here, we consider the same environment used in the previous example in Sec. III A 1 but with a water depth of 50 m. The thickness of the ice layer is chosen as 10 m based on the maximum size of the ice keel shown in Fig. 4. The following analysis also supports the initial discussion on the applicability of effective ice representations in Secs. III A and III B. In this case, the source is placed 1 m close to the ice layer such that the elastic mode in the ice layer can be excited, with a source frequency of 100 Hz. Figure 14(b) displays the dispersion curves for the 50 m-deep waveguide, which is calculated by SBFEM. The phase velocities of the first seven modes at 100 Hz are annotated by the dashed blue lines, with their values detailed in Table I.

We now identify the waveguide modes in wavenumber spectra by matching their phase velocities computed by SBFEM. Figure 15 shows the wavenumber spectrum in the horizontal wavenumber (k_x)-depth domain. Medium wavenumbers k_p , k_w , and k_s are shown in

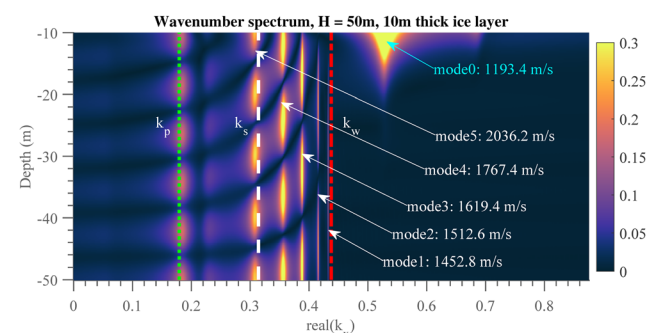


FIG. 15. Wavenumber-domain spectra calculated using the sound pressure output from ESM-SUBICE for the 50 m-deep waveguide covered by a 10 m-thick ice layer. Other parameters are the same as those in Sec. III A 1.

dashed vertical lines on this figure to divide the wavenumber spectrum into three regions: a) continuous spectrum ($k_x < k_s$) where waves leak to the seafloor and ice layer, b) the discrete spectrum ($k_s < k_x < k_w$) that contains poles corresponding to propagating modes in the water column, and c) the evanescent spectrum, which represents wave components exponentially decaying in the vertical in both water and seabed. When the elastic ice layer is considered, interface waves pertain to the evanescent spectrum, inducing additional poles corresponding to the plate flexural modes of the ice layer. Figure 15 exhibits visible modal-like patterns, indicating that modes 1–4 are propagating modes, while modes 5 and 6 are leaky. The plate flexural modes of the ice layer (mode 0) are represented by the interface-wave mode pattern to the right of k_w exhibiting its evanescent character in water. All these features agree well with the phase velocities given by SBFEM (Table I), thus confirming that the ESM-SUBICE correctly describes the behavior of each waveguide mode.

After identifying waveguide modes in wavenumber spectra, we further discuss the effect of ice elasticity on propagation and scattering based on the wavenumber-spectrum analysis, which directly gives insights into the underlying waveguide physics. Figure 15 shows the wavenumber spectra for different waveguide parameters. By comparing Figs. 15 and 16(a), one can observe that, as the ice thickness reduces from 10 to 3 m, mode 5 changes from propagating to leaky, and singularities corresponding to modes 1 and 2 become weak. More importantly, the case of the 3 m-thick ice layer barely shows the poles corresponding to the plate flexural modes. This means that, as the ice thickness increases with range, the low-order modal coupling between acoustic and elastic waves may occur, potentially exciting the plate flexural modes of the ice layer that further induce the shear-wave attenuation and the supercritical incidence of the ice-borne scattering to the bottom (the coupling between the leaky elastic modes and the high-order modes, as discussed in Secs. III A 2 and B 2). Only low-order elastic modes can be excited since the ice is thin compared with water depth. Such acoustic-elastic coupling effects result in the TL discrepancies in Fig. 9(a).

Figure 16(b) shows the wavenumber spectrum for a 300 m deep waveguide covered by a 10 m-thick ice layer. Compared with Fig. 15, Fig. 16(b) exhibits more high-order modes propagating at large grazing angles relative to the seafloor, meaning that the waveguide behavior in deep water is dominated by the high-order mode rather than the

TABLE I. Phase velocity of the first six modes labeled in Fig. 14(b) at 100 Hz.

Mode 0	Mode 1	Mode 2	Mode 3	Mode 4	Mode 5	
Phase velocity (m/s)	1225.3	1458.4	1514.4	1611.7	1742.1	2028.1

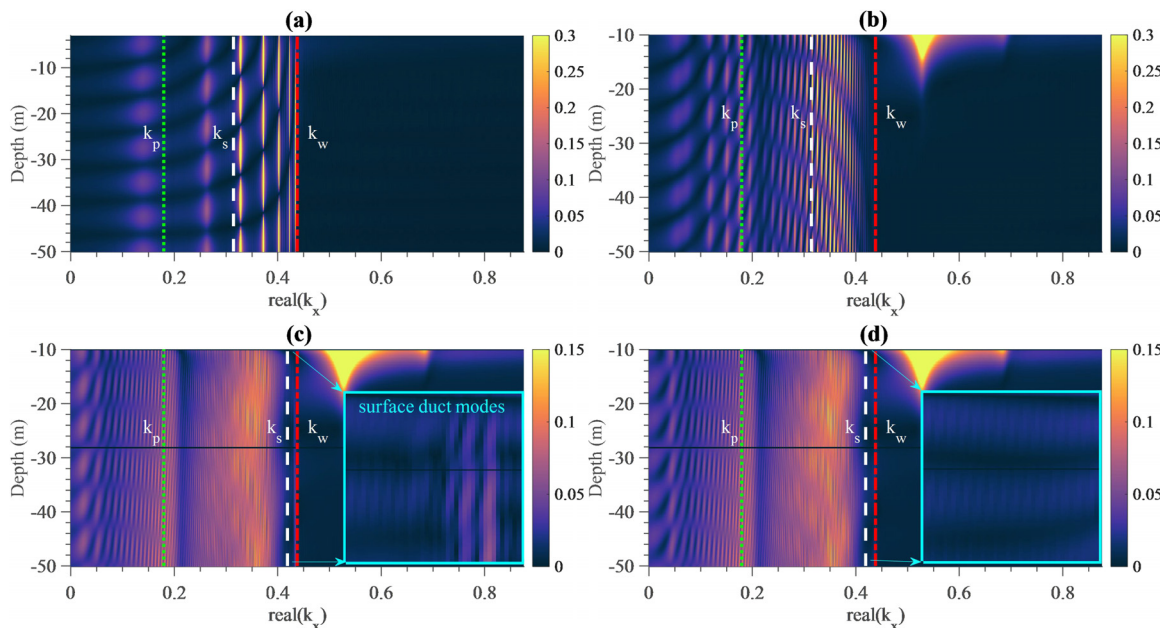


FIG. 16. Wavenumber-domain spectra calculated using the sound pressure output from ESM-SUBICE for (a) the 50 m-deep waveguide covered by a 3 m-thick ice layer and (b) the 300 m-deep waveguide covered by a 10 m-thick ice layer. Other parameters are the same as those in Sec. IIIA 1. (c) and (d) The wavenumber-domain spectra for the up-refractive and iso-velocity deep-water environments simulated in Sec. IIIB 1, respectively, but with a 10 m thick ice layer. (a) $H = 50$ m, 3 m thick ice, (b) $H = 300$ m, 10 m thick ice, (c) $H = 1200$ m, 10 m thick ice, up-refractive, and (d) $H = 1200$ m, 10 m thick ice, iso-velocity.

acoustic-elastic coupling between the propagating and elastic modes. This explains why the effective ice representation is valid for deep-water environments. The wavenumber spectra for different types of seafloors are not given here to save space, the features of which can be inferred very easily based on the above analyses. Soft seabed only supports a few low-order modes to propagate in the waveguide, and such a waveguide can be approximated as a leaky half space. Therefore, the acoustic-elastic coupling is relatively weak in the ice-covered ocean with a soft seabed. This explains why the effective ice representation is valid for soft seabeds.

Figures 16(c) and 16(d), then, show the wavenumber-domain spectra for the up-refractive and iso-velocity deep-water environments considered in Sec. IIIB 1, respectively, but with a 10 m-thick ice layer. These spectra are almost identical, where leaky modes are dominant due to the deep water. Two visible differences between these spectra are: a) distributions of leaky modes to the left of k_p and b) surface duct modes supported by the up-refractive sound speed profile [shown in the magnified figure in Fig. 16(c)]. The surface duct modes contribute to the surface channel, within which sound waves are trapped. They intensify the acoustic-elastic interaction, potentially causing the coupling between the propagating and elastic modes, as explained in Sec. IIIB 1. Therefore, the effective ice representation is valid when the surface duct modes are leaky.

D. Pulse propagation in the time domain

Pulse propagation is now considered to qualitatively study scattering from the rough ice-water interface in the time domain. The pulse bandwidth is 60 Hz centered at 75 Hz, and the acoustic environment is the same as that for Sec. IIIA. Figure 17 (Multimedia view)

shows the time evolution of pulse propagation. At the beginning ($t = 0.13$ s), a clear front of head waves can be observed, forming a line segment starting from a P wave in the ice layer interacting tangentially with the surface-reflected wavefront. The P wave travels ahead of the S wave at a faster speed, which is almost three times the water sound speed. At $t = 1.8$ s, more pronounced reflected patterns are observable along with visible reverberations due to the rough ice layer. At $t = 3.5$ s, the number of reflections increases, and scattering effects are apparent. At $t = 6.3$ s, several visible “tails” following each path indicate scattering from the rough air-ice interface. For comparison, Fig. 18 (Multimedia view) also gives the corresponding results with flat ice, in which several pieces of evidence supporting rough scattering are absent.

To illustrate the scattering effect in more detail, Fig. 19 shows stacked time series vs range at $z = -50$ m in the rough and flat cases. For flat ice, separated wave packets tend to be observed with increasing range; these correspond to different propagation modes (dispersion behavior), which travel at different group velocities (higher modes travel at lower speeds). Therefore, the received signals exhibit more distinct wave packets at longer than shorter ranges. Note that between two distinct wave packets, the received signal is almost zero in the absence of rough scattering from ice keels. Conversely, significant distortions in wave packets are seen in Fig. 19(a) at short ranges (1.5–5.5 km) due to scattering. Moreover, the time signal exhibits apparent reverberations at greater distances, spreading over the distinct wave packets observed in the flat ice case.

E. Discussion on numerical efficiency

We now discuss the numerical efficiency of ESM-SUBICE in comparison with direct Multiphysics FEM. First, the numerical cost of

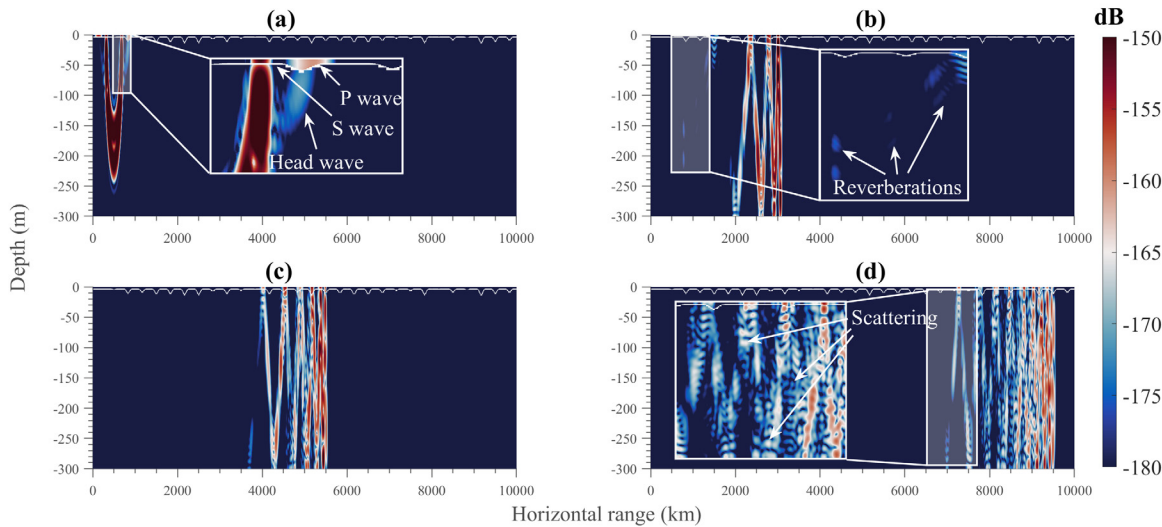


FIG. 17. Time evolution of a pulse in the iso-velocity waveguide with a rough ice layer shown in Fig. 4 at (a) 0.13 s, (b) 1.8 s, (c) 3.5 s, and (d) 6.3 s. Multimedia view: <https://doi.org/10.1063/5.0144919.1>

the proposed method depends on the unknown number (UN) regarding all ESs involved in reproducing the wave field. In our implementations, N_{UN} is determined by a one-sixth acoustic wavelength rule to discretize the waveguide boundary. Given the UN regarding each set of ES in ESM-SUBICE, the corresponding numeral cost is $O[(2I + 1)N_{\text{UN}}^{2-3}]$, in which the evaluation of the dense coefficient matrix involving the complex image method costs $O(QN_{\text{UN}})$ operations, where Q is the order of the image source. Generally, $Q = 5$ provides acceptable accuracy for most fluid seaboards, according to previous numerical tests.^{37,40}

The FEM couples the solid mechanics and pressure acoustics, requiring discretization of the whole space, including the perfectly matched layers to absorb out-going waves at each end of the

waveguide and the lower half-space of the seabed. The FEM discretization scheme uses the same one-sixth rule as for ESM-SUBICE in the fluid domain.^{42,43} Given the degrees of freedom (DOF) of FEM, the corresponding numerical cost is $O(N_{\text{DOF}}^{2-3})$. On the basis of the BI and volume discretization for treating the same problem, it is anticipated that N_{DOF} will be significantly larger than N_{UN} .

Table II lists the numerical costs and average computation times required by ESM-SUBICE and FEM in each simulation. As expected, N_{DOF_m} is 7–8 orders of magnitude greater than N_{UN} . Therefore, FEM is more numerically expensive than ESM-SUBICE, taking more than twice the computation time. This analysis demonstrates the high efficiency of ESM-SUBICE when compared with full-wave FEM.

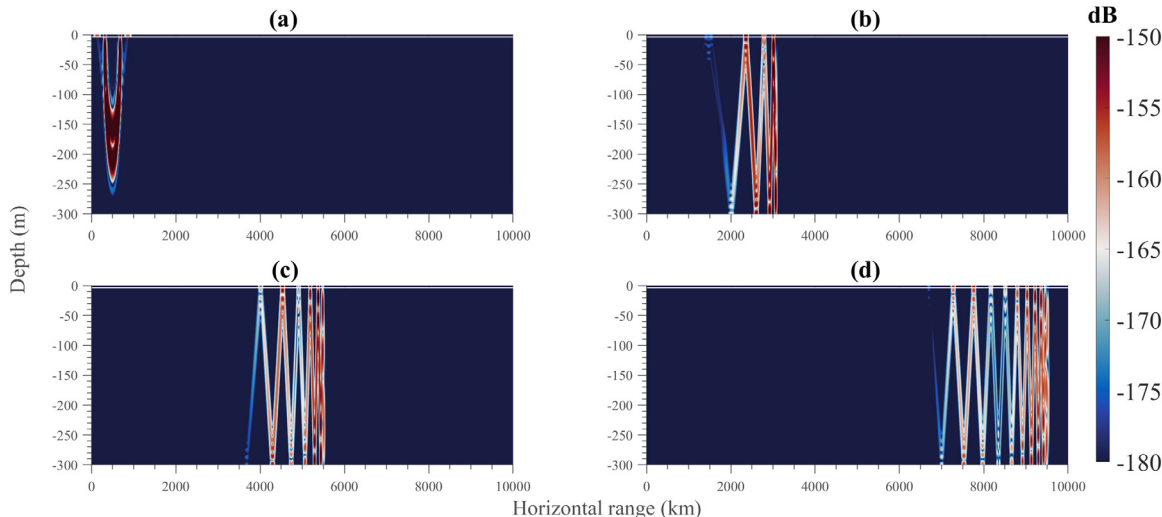


FIG. 18. Time evolution of a pulse in an iso-velocity waveguide with flat ice cover at (a) 0.13 s, (b) 1.8 s, (c) 3.5 s, and (d) 6.3 s. Multimedia view: <https://doi.org/10.1063/5.0144919.2>

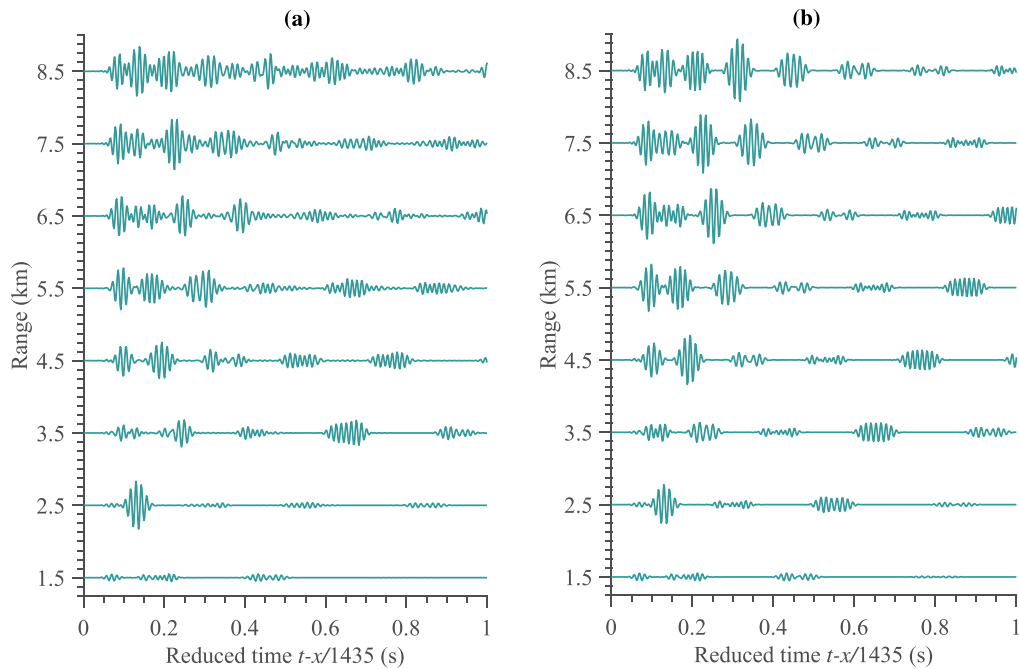


FIG. 19. Time signal vs range at a depth of $z = -50$ m in the (a) rough and (b) flat ice cases. The time axis is reduced time, and all traces are multiplied by \sqrt{x} to compensate for geometric spreading.

IV. CONCLUSIONS

This article has presented an ESM-based model, ESM-SUBICE, for predicting elastic- and acoustic-wave propagation in ice-covered ocean acoustic environments. ESM-SUBICE solves the exact governing equations for acoustic–elastic propagation by expressing the wave solution in terms of field superposition produced by several sets of ESs. In the elastic ice, four sets of ESs are used to reproduce the scalar and shear potentials. The ocean is divided into layers, each of which requires two sets of ESs. All sets of ESs are then coupled by enforcing the strict air–ice and ice–water boundary conditions and continuity conditions across each interface between two adjacent water layers. By further using the water–seabed half-space Green’s function, the computational complexity regarding the water–seabed interface is reduced. The nature of field decomposition inherited in ESM-SUBICE allows one to study the compressional- and shear-wave fields individually, providing insights into waveguide physics.

Simulations demonstrated ESM-SUBICE’s validity and capability for predicting wave propagation in complex ice-covered ocean

acoustic environments. Benchmarking against FEM validated ESM-SUBICE, confirming that it provides high-quality solutions. ESM-SUBICE was further implemented to simulate wave propagation in an ice-covered, up-refractive deep ocean with and without a Gaussian seamount. The enhanced surface-duct scattering and the modal cutoff associated with up-slope propagation indicate that the results are reasonable. Due to the high numerical efficiency of ESM-SUBICE, pulse propagation was used to qualitatively investigate the scattering mechanism in an iso-velocity ocean covered by an ice layer with keels.

The applicability of effective ice representations was examined, and the results suggest that the fluid representation is adequate for deep-water environments where the seabed is soft and the surface duct effect is insignificant. This article has demonstrated the potential of ESM-SUBICE to be a useful tool in sub-ice acoustic communication, localization, and detection. Future work will focus on extending ESM-SUBICE to handle fully 3D scenarios.

The original contribution of this work is given in the following:

- A meshless, wave-based sound propagation model in ice-covered ocean environments is described using the equivalent-source method, which can fast solve the full-wave field, including the shear potentials in the ice. The model fully accounts for the effects of ice elasticity on the sub-ice sound propagation. It is highly suitable for a multi-layer sub-ice ocean environment compared with a classical coupled normal mode code commonly used for handling a three-layer waveguide. Also, its nature of meshless and boundary-integral makes it more applicable to Monte Carlo simulations or parameter sweeps compared with models based on volume discretization.

TABLE II. Analysis of the numerical cost and average computation time required by ESM-SUBICE and FEM.

	300-m-deep waveguide		1200-m-deep waveguide	
	FEM	ESM-SUBICE	FEM	ESM-SUBICE
$N_{\text{UN}}/N_{\text{DOF}}$	4 158 682	20 910	13 022 662	54 366
O	$O(10^{19})$	$O(10^{12})$	$O(10^{21})$	$O(10^{14})$
t	4 min 40 s	1 min 45 s	11 min	6 min

- The effect of ice elasticity on propagation and scattering is fundamentally discussed and interpreted by a wavenumber-spectrum analysis, in which each waveguide mode is identified by tracking its phase velocity computed by SBFEM. This gives insights into the underlying waveguide physics from the modal perspective. A significant feature of ice is revealed: Ice elasticity may not be the dominant loss mechanism for sub-ice sound propagation when the high-order propagating modes are supported and the surface-duct modes are leaky. This may be useful for the equivalent ice representation required for a fluid sound propagation model, especially for 3D modeling.

ACKNOWLEDGMENTS

This work was supported by the National Natural Science Foundation of China (Grant No. 52101387). The authors thank the two anonymous reviewers whose helpful comments and suggestions have greatly improved the manuscript.

AUTHOR DECLARATIONS

Conflict of Interest

The authors have no conflicts to disclose.

Author Contributions

Tengjiao He: Conceptualization (lead); Investigation (lead); Methodology (lead); Software (lead); Validation (lead); Writing – original draft (lead); Writing – review & editing (lead). **Bin Wang:** Conceptualization (equal); Methodology (equal); Supervision (equal); Writing – review & editing (equal). **Shengyu Tang:** Resources (equal); Software (equal); Validation (equal); Writing – review & editing (equal). **Fulin Zhou:** Software (equal); Supervision (equal); Validation (equal). **Shiqi Mo:** Conceptualization (supporting); Methodology (supporting); Supervision (supporting). **Erzheng Fang:** Conceptualization (supporting).

DATA AVAILABILITY

Data sharing is not applicable to this article as no new data were created or analyzed in this study.

APPENDIX: DERIVATION OF THE POTENTIAL BASED GOVERNING EQUATION

The homogeneous displacement equation of motion in a homogeneous and isotropic elastic medium is given by¹⁷

$$(\lambda_{sh} + \mu) \nabla (\nabla \cdot \mathbf{u}) + \mu \nabla^2 \mathbf{u} = \rho \ddot{\mathbf{u}}, \quad (\text{A1})$$

where ρ is the medium density, “ $\ddot{\cdot}$ ” denotes $\frac{\partial^2}{\partial t^2}$, and the displacement field \mathbf{u} has the vector form of

$$\mathbf{u} = \frac{1}{\omega^2 \rho} \left[\nabla \Phi_p + \nabla \times \vec{\Psi}_{sh} \right], \quad (\text{A2})$$

where Φ_p and $\vec{\Psi}_{sh}$ are the scalar and vector potentials, respectively. By substituting Eq. (A2) back in Eq. (A1), the left-hand side (LHS) of Eq. (A1) can be written as follows

$$\begin{aligned} \text{LHS} &= (\lambda_{sh} + \mu) \nabla (\nabla \cdot (\nabla \Phi_p + \nabla \times \vec{\Psi}_{sh})) \\ &\quad + \mu \nabla^2 (\nabla \Phi_p + \nabla \times \vec{\Psi}_{sh}) \\ &= \nabla (\lambda_{sh} + \mu) \left[\nabla \cdot (\nabla \Phi_p + \nabla \times \vec{\Psi}_{sh}) \right] \\ &\quad + \mu \nabla (\nabla^2 \Phi_p) + \mu \nabla^2 (\nabla \times \vec{\Psi}_{sh}) \\ &= \nabla (\lambda_{sh} + \mu) (\nabla \cdot \nabla \Phi_p) + \nabla \mu (\nabla^2 \Phi_p) \\ &\quad + \mu \left[\nabla (\nabla \cdot (\nabla \times \vec{\Psi}_{sh})) - \nabla \times \nabla \times (\nabla \times \vec{\Psi}_{sh}) \right] \\ &= \nabla (\lambda_{sh} + 2\mu) (\nabla^2 \Phi_p) - \mu \nabla \times \nabla \times (\nabla \times \vec{\Psi}_{sh}). \end{aligned} \quad (\text{A3})$$

The above derivation uses the relation $\nabla \cdot (\nabla \times \vec{\Psi}_{sh}) = 0$ and $\nabla \times (\nabla \times \vec{\Psi}_{sh}) = \nabla (\nabla \cdot \vec{\Psi}_{sh}) - \nabla^2 \vec{\Psi}_{sh}$. Similarly, the right-hand side (RHS) of Eq. (A1) is rewritten as

$$\text{RHS} = \rho \nabla \ddot{\Phi}_p + \rho \nabla \times \ddot{\vec{\Psi}}_{sh}. \quad (\text{A4})$$

A set of wave equations of the scalar and vector potentials can be obtained by substituting Eqs. (A3) and (A4) back in Eq. (A1), and after some rearranging, this yields

$$\begin{cases} \frac{\lambda_{sh} + 2\mu}{\rho} \nabla^2 \Phi_p = \ddot{\Phi}_p \\ -\frac{\mu}{\rho} \nabla \times (\nabla \times \vec{\Psi}_{sh}) = \ddot{\vec{\Psi}}_{sh}. \end{cases} \quad (\text{A5})$$

When considering the 2D case, $\vec{\Psi}_{sh} = [0, \Psi_{sh}, 0]$. The 2D Helmholtz equations of the scalar and vector potentials, then, can be derived by the use of the frequency-time Fourier transform pair, and this yields

$$\begin{cases} [\nabla^2 + k_p^2] \Phi_p = 0 \\ [\nabla^2 + k_{sh}^2] \Psi_{sh} = 0. \end{cases} \quad (\text{A6})$$

Equation (A6) gives the same governing equations as in Eq. (1). Note that the above derivation and the boundary conditions defined in Eq. (2) indicate that the potential-based governing equations used in this article are the exact wave equation governing the acoustic–elastic propagation in an ice-covered waveguide.

REFERENCES

- T. F. Duda, “Acoustic signal and noise changes in the Beaufort sea pacific water duct under anticipated future acidification of Arctic ocean waters,” *J. Acoust. Soc. Am.* **142**, 1926–1933 (2017).
- G. Hope, H. Sagen, E. Storheim, H. Hobæk, and L. Freitag, “Measured and modeled acoustic propagation underneath the rough arctic sea-ice,” *J. Acoust. Soc. Am.* **142**, 1619–1633 (2017).
- M. S. Ballard, M. Badiey, J. D. Sagers, J. A. Colosi, A. Turgut, S. Pecknold, Y.-T. Lin, A. Proshutinsky, R. Krishfield, P. F. Worcester *et al.*, “Temporal and spatial dependence of a yearlong record of sound propagation from the Canada Basin to the Chukchi shelf,” *J. Acoust. Soc. Am.* **148**, 1663–1680 (2020).
- V. G. Petnikov, V. A. Grigorev, A. A. Lunkov, and D. D. Sidorov, “Modeling underwater sound propagation in an Arctic shelf region with an inhomogeneous bottom,” *J. Acoust. Soc. Am.* **151**, 2297–2309 (2022).
- A. Širović, J. A. Hildebrand, S. M. Wiggins, M. A. McDonald, S. E. Moore, and D. Thiele, “Seasonality of blue and fin whale calls and the influence of sea ice in the Western Antarctic Peninsula,” *Deep Sea Res. Part II* **51**, 2327–2344 (2004).

- ⁶J. Delarue, M. Laurinolli, and B. Martin, "Acoustic detections of beluga whales in the Northeastern Chukchi sea, July 2007 to July 2008," *Arctic* **64**, 15–24 (2011).
- ⁷R. E. Keenan and I. Dyer, "Noise from Arctic ocean earthquakes," *J. Acoust. Soc. Am.* **75**, 819–825 (1984).
- ⁸D. M. Farmer and Y. Xie, "The sound generated by propagating cracks in sea ice," *J. Acoust. Soc. Am.* **85**, 1489–1500 (1989).
- ⁹M. C. Zeh, M. S. Ballard, O. Glowacki, G. B. Deane, and P. S. Wilson, "Model-data comparison of sound propagation in a glacierized fjord with a simulated brash ice surface," *J. Acoust. Soc. Am.* **151**, 2367–2377 (2022).
- ¹⁰J. K. Lewis and W. W. Denner, "Arctic ambient noise in the Beaufort sea: Seasonal space and time scales," *J. Acoust. Soc. Am.* **82**, 988–997 (1987).
- ¹¹J. K. Lewis and W. W. Denner, "Arctic ambient noise in the Beaufort sea: Seasonal relationships to sea ice kinematics," *J. Acoust. Soc. Am.* **83**, 549–565 (1988).
- ¹²D. Mann, P. Cott, and B. Horne, "Under-ice noise generated from diamond exploration in a Canadian sub-Arctic lake and potential impacts on fishes," *J. Acoust. Soc. Am.* **126**, 2215–2222 (2009).
- ¹³G. Jin, J. F. Lynch, R. Pawlowicz, and P. Worcester, "Acoustic scattering losses in the Greenland Sea marginal ice zone during the 1988–89 tomography experiment," *J. Acoust. Soc. Am.* **96**, 3045–3053 (1994).
- ¹⁴A. N. Gavrilov and P. N. Mikhalevsky, "Low-frequency acoustic propagation loss in the Arctic ocean: Results of the Arctic climate observations using underwater sound experiment," *J. Acoust. Soc. Am.* **119**, 3694–3706 (2006).
- ¹⁵L. Freitag, P. Koski, A. Morozov, S. Singh, and J. Partan, "Acoustic communications and navigation under Arctic ice," in *Proceedings of the 2012 Oceans* (IEEE, 2012), pp. 1–8.
- ¹⁶S. Cang, J. Swärd, X. Sheng, and A. Jakobsson, "Toeplitz-based blind deconvolution of underwater acoustic channels using wideband integrated dictionaries," *Signal Process.* **179**, 107812 (2021).
- ¹⁷F. B. Jensen, W. A. Kuperman, M. B. Porter, and H. Schmidt, *Computational Ocean Acoustics* (Springer Science and Business Media, 2011).
- ¹⁸B. Simon, M. Isakson, and M. Ballard, "Modeling acoustic wave propagation and reverberation in an ice covered environment using finite element analysis," in *Proceedings of Meetings on Acoustics 175ASA* (Acoustical Society of America, 2018), Vol. 33, p. 070002.
- ¹⁹M. B. Porter and H. P. Bucker, "Gaussian beam tracing for computing ocean acoustic fields," *J. Acoust. Soc. Am.* **82**, 1349–1359 (1987).
- ²⁰J. D. Sagers, M. S. Ballard, and M. Badiey, "Investigating the effects of ocean layering and sea ice cover on acoustic propagation in the beaufort sea," in *Proceedings of Meetings on Acoustics 170ASA* (Acoustical Society of America, 2015), Vol. 25, p. 005003.
- ²¹W. A. Kuperman and H. Schmidt, "Self-consistent perturbation approach to rough surface scattering in stratified elastic media," *J. Acoust. Soc. Am.* **86**, 1511–1522 (1989).
- ²²J. M. Collis, S. D. Frank, A. M. Metzler, and K. S. Preston, "Elastic parabolic equation and normal mode solutions for seismo-acoustic propagation in underwater environments with ice covers," *J. Acoust. Soc. Am.* **139**, 2672–2682 (2016).
- ²³S. D. Frank and A. N. Ivakin, "Long-range reverberation in an Arctic environment: Effects of ice thickness and elasticity," *J. Acoust. Soc. Am.* **143**, EL167–EL173 (2018).
- ²⁴M. D. Collins, "A split-step Padé solution for the parabolic equation method," *J. Acoust. Soc. Am.* **93**, 1736–1742 (1993).
- ²⁵J. F. Lingevitch and K. D. LePage, "Parabolic equation simulations of reverberation statistics from non-Gaussian-distributed bottom roughness," *IEEE J. Oceanic Eng.* **35**, 199–208 (2010).
- ²⁶J. R. Fricke, "Acoustic scattering from elemental Arctic ice features: Numerical modeling results," *J. Acoust. Soc. Am.* **93**, 1784–1796 (1993).
- ²⁷Z. Zhang and C. Tindle, "Improved equivalent fluid approximations for a low shear speed ocean bottom," *J. Acoust. Soc. Am.* **98**, 3391–3396 (1995).
- ²⁸M. S. Ballard, "Three-dimensional acoustic propagation effects induced by the sea ice canopy," *J. Acoust. Soc. Am.* **146**, EL364–EL368 (2019).
- ²⁹T. F. Duda, W. G. Zhang, and Y.-T. Lin, "Effects of Pacific summer water layer variations and ice cover on Beaufort Sea underwater sound ducting," *J. Acoust. Soc. Am.* **149**, 2117–2136 (2021).
- ³⁰H. Tu, Y. Wang, Y. Zhang, H. Liao, and W. Liu, "Parallel numerical simulation of weakly range-dependent ocean acoustic waveguides by adiabatic modes based on a spectral method," *Phys. Fluids* **35**, 017119 (2023).
- ³¹H. Tu, Y. Wang, C. Yang, W. Liu, and X. Wang, "A Chebyshev–Tau spectral method for coupled modes of underwater sound propagation in range-dependent ocean environments," *Phys. Fluids* **35**, 037113 (2023).
- ³²G. H. Koopmann, L. Song, and J. B. Fahnline, "A method for computing acoustic fields based on the principle of wave superposition," *J. Acoust. Soc. Am.* **86**, 2433–2438 (1989).
- ³³L. Godinho, A. Tadeu, and F. Branco, "3D acoustic scattering from an irregular fluid waveguide via the BEM," *Eng. Anal. Boundary Elem.* **25**, 443–453 (2001).
- ³⁴A. Pereira, A. Tadeu, L. Godinho, and J. Santiago, "2.5 D BEM modeling of underwater sound scattering in the presence of a slippage interface separating two flat layered regions," *Wave Motion* **47**, 676–692 (2010).
- ³⁵C. Li, B. K. Campbell, Y. Liu, and D. K. Yue, "A fast multi-layer boundary element method for direct numerical simulation of sound propagation in shallow water environments," *J. Comput. Phys.* **392**, 694–712 (2019).
- ³⁶A. T. Abawi and M. B. Porter, "Propagation in an elastic wedge using the virtual source technique," *J. Acoust. Soc. Am.* **121**, 1374–1382 (2007).
- ³⁷T. He, V. F. Humphrey, S. Mo, and E. Fang, "Three-dimensional sound scattering from transversely symmetric surface waves in deep and shallow water using the equivalent source method," *J. Acoust. Soc. Am.* **148**, 73–84 (2020).
- ³⁸T. He, S. Mo, W. Guo, and E. Fang, "Modeling propagation in shallow water with the range-dependent sea surfaces and fluid seabeds using the equivalent source method," *J. Acoust. Soc. Am.* **149**, 997–1011 (2021).
- ³⁹T. He, S. Mo, E. Fang, M. Wang, and R. Zhang, "Modeling three-dimensional underwater acoustic propagation over multi-layered fluid seabeds using the equivalent source method," *J. Acoust. Soc. Am.* **150**, 2854–2864 (2021).
- ⁴⁰J. A. Fawcett, "Complex-image approximations to the half-space acousto-elastic Green's function," *J. Acoust. Soc. Am.* **108**, 2791–2795 (2000).
- ⁴¹J. A. Fawcett, "A method of images for a penetrable acoustic waveguide," *J. Acoust. Soc. Am.* **113**, 194–204 (2003).
- ⁴²M. J. Isakson and N. P. Chotiros, "Finite element modeling of acoustic scattering from fluid and elastic rough interfaces," *IEEE J. Oceanic Eng.* **40**, 475–484 (2014).
- ⁴³M. J. Isakson and N. P. Chotiros, "Finite element modeling of reverberation and transmission loss in shallow water waveguides with rough boundaries," *J. Acoust. Soc. Am.* **129**, 1273–1279 (2011).
- ⁴⁴T. He, B. Wang, S. Mo, and E. Fang, "Predicting range-dependent underwater sound propagation from structural sources in shallow water using coupled finite element/equivalent source computations," *Ocean Eng.* **272**, 113904 (2023).
- ⁴⁵S. Tang, G. Zhu, X. Wang, and J. Yin, "Determination of modes in the ice–water bi-layer waveguide," *J. Theor. Comput. Acoust.* (published online 2022).